Source Sector and Region Contributions to BC and $PM_{2.5}$ in Central Asia

S. Kulkarni[1*], N. Sobhani[1,2], J. P. Miller-Schulze[3,4], M. M. Shafer[3,4,], J. J. Schauer[3,4], P. A. Solomon[5], P. E. Saide[1], S. N. Spak[6,1], Y. F. Cheng[1**], H.A.C. Denier van der Gon[7], Z. Lu[8], D.G. Streets[8], G. Janssens-Maenhout[9], C. Wiedinmyer[10], J. Lantz[11], M. Artamonova[12], B. Chen[13], S. Imashev[13], L. Sverdlik[13], J. T. Deminter[3], B. Adhikary[1***], A. D'Allura[14], C. Wei[1****], and G. R. Carmichael[1,2]

[1]Center for Global and Regional Environmental Research, University of Iowa, Iowa City, IA

[2]Department of Chemical & Biochemical Engineering, The University of Iowa, Iowa City, IA 52242, USA

[3] Wisconsin State Laboratory of Hygiene, 2601 Agriculture Drive, Madison, WI 53718, USA

[4] Environmental Chemistry and Technology Program, 660 North Park St, University of Wisconsin, Madison, WI 53706, USA

[5] U.S. EPA, Office of Research & Development, Las Vegas, NV 89193, USA

[6] Public Policy Center, University of Iowa, 223 South Quadrangle, Iowa City, IA 52242

[7] TNO, Princetonlaan 6, 3584 CB Utrecht, The Netherlands

[8]Decision and Information Sciences Division, Argonne National Laboratory, Argonne, IL, USA

[9]European Commission, Joint Research Centre, IES, 21027 Ispra, Italy

[10]National Center for Atmospheric Research, Boulder, Colorado, USA

[11] U.S. EPA, Office of Radiation and Indoor Air, Las Vegas, NV 89193, USA

[12] Institute of Atmospheric Physics, 109017 Moscow, Russia

[13] Kyrgyz-Russian Slavic University, 44 Kievskaya Str., Bishkek 720000, Kyrgyzstan

[14]ARIANET, via Gilino 9, 20128 Milan, Italy

[*] now at: California Air Resource Board, Sacramento, CA USA

**now at: Multiphase chemistry department, Max Planck Institute for Chemistry, Mainz 55128, Germany

*** now at: International Centre for Integrated Mountain Development (ICIMOD), GPO Box 3226, Kathmandu, Nepal

****now at US EPA, Atmospheric Modeling and Analysis Division, Research Triangle Park, NC USA

Correspondence to: N. Sobhani (negin-sobhani@uiowa.edu) and G.R. Carmichael (gcarmich@engineering.uiowa.edu)

Abstract

Particulate matter (PM) mass concentrations, seasonal cycles, source sector and source region contributions in Central Asia (CA) are analyzed for the period April 2008-July 2009 using the Sulfur Transport and dEposition Model (STEM) chemical transport model and modeled meteorology from the Weather Research and Forecasting (WRF) model. Predicted Aerosol Optical Depth (AOD) values (annual mean value ~0.2) in CA vary seasonally with lowest values in the winter. Surface $PM_{2.5}$ concentrations (annual mean value ~10 $\mu g/m^3$) also exhibit a seasonal cycle, with peak values and largest variability in the spring/summer, and lowest values and variability in the winter (hourly values from 2 – 90 $\mu g/m^3$). Surface concentrations of black carbon (BC) (mean value ~0.1 $\mu g/m^3$) show peak values in the winter. The simulated values are compared to surface measurements of AOD, and $PM_{2.5}$, PM_{10}, BC, organic carbon (OC) mass concentrations at two regional sites in the Kyrgyz Republic (Lidar Station Teplokluchenka (LST) and Bishkek). The predicted values of AOD and PM mass concentrations and their seasonal cycles are fairly well captured. The carbonaceous aerosols are underpredicted in winter, and analysis suggests that the winter heating emissions are underestimated in the current inventory.

Dust, from sources within and outside CA, is a significant component of the PM mass and drives the seasonal cycles of PM and AOD. On an annual basis, the power and industrial sectors are found to be the most important contributors to the anthropogenic portion of $PM_{2.5}$. Residential combustion and transportation are shown to be the most important sectors for BC. Biomass burning within and outside the region also contributes to elevated PM and BC concentrations. The analysis of the transport pathways and the variations in particulate matter mass and

composition in CA demonstrate that this region is strategically located to characterize regional and intercontinental transport of pollutants. Aerosols at these sites are shown to reflect dust, biomass burning and anthropogenic sources from Europe, South, East and CA, and Russia depending on the time period.

Simulations for a reference 2030 emission scenario based on pollution abatement measures already committed to in current legislation show that $PM_{2.5}$ and BC concentrations in the region increase, with BC growing more than $PM_{2.5}$ on a relative basis. This suggests that both the health impacts and the climate warming associated with these particles may increase over the next decades unless additional control measures are taken. The importance of observations in CA to help characterize the changes that are rapidly taking place in the region are discussed.

1. Introduction

Central Asia (CA), a region of republics located between Europe and Asia, faces severe environmental problems, with origins dating back to the 1960s and best symbolized by the Aral Sea catastrophe (Whish-Wilson, 2002). The Aral Sea has shrunk to only about 30 percent of its 1960 volume and roughly half its geographical size due to diversion of water for crop cultivation and other purposes. The resulting desertification of the lake-bed has resulted in extensive dust storms from the region, which have impacted the surrounding agriculture, ecosystem, and the population's health.

The 2012 Environmental Performance Index (EPI), which tracks performance of 132 countries across a variety of environmental and ecosystem vitality indicators, ranked CA countries among the weakest performers (Kazakhstan 129, Uzbekistan 130, Turkmenistan 131, Tajikistan 121, and Kyrgyzstan 101) (Emerson et al., 2012). CA and the surrounding areas are developing quickly and air pollution emissions are projected to increase significantly for the next several decades (Shindell et al., 2012). In recognition of the need to improve the environmental conditions in the region five CA countries have formulated the Framework Convention on Preservation of Environment for Sustainable Development of CA (UNEP, 2006).

Despite the awareness of the environmental conditions, it remains an understudied region and there is a general lack of air pollution observations within CA. Furthermore the recent assessment of the intercontinental transport of pollution (HTAP, 2010) has indicated that the major transport pathway of pollution from Europe to Asia is via low altitude flows passing through CA. The magnitude of the pollution transport from Europe to Asia is highly uncertain in large part due to the lack of observations of pollutants along this pathway. To help better characterize the air pollution levels and the transport pathways in the region a study was

undertaken between Russia, Kyrgyz Republic, and USA scientists to observe and model aerosols in the region. Measurements of particulate matter (PM) mass and composition were taken at two locations in the Kyrgyz Republic (Lidar Station Teplokluchenka (LST) and Bishkek) and modeling analysis was performed to assess the contributions of local, regional and distant sources to the PM concentrations in the region (Miller-Schulze et al., 2012, Chen et al., 2012, 2013).

In this paper we present a modeling analysis of $PM_{2.5}$, PM_{10}, ($PM_{2.5}$ refers to particles in the size range of less than 2.5 μm aerodynamic diameter (AD) and PM_{10} refers to particles in the size range of less than 10 μm AD), black carbon (BC) and organic carbon (OC) mass concentrations and aerosol optical depth (AOD) over the time period of April 2008 to July 2009. The Sulfur Transport and dEpostion Model (STEM), a hemispheric chemical transport model (D'Allura et al., 2011), is used to estimate spatial and temporal variations in PM in CA, and to assess the contributions to PM from wind-blown dust, open biomass burning, and anthropogenic sources, and different geographical source regions and source sectors (transportation, power, industry and residential). The simulated values are compared to surface measurements of AOD, $PM_{2.5}$, PM_{10}, BC, OC mass concentrations at the two regional sites in CA. The transport of aerosols into CA is also explored through three dimensional backward trajectory analysis. Transport from CA and their impacts on downwind areas are also analyzed via forward trajectory analysis. Finally we present results of how the PM concentrations may change in the future using emission scenarios for 2030 that reflect possible air quality and climate policies.

2. Data and Methods

2.1. Observations

Surface observations from two sites established in the Kyrgyz Republic to measure PM concentrations and AOD in CA are used in the analysis. The locations of the Bishkek (42°40'46.65"N, 74°41'38.13"E, elevation 1743 above sea level (ASL)) and LST (42°27'49.38"N, 78°31'44.17"E, elevation 1921 m ASL) sites are denoted by circle and triangle markers, respectively, in Fig. 1. Both sampling sites are in mountain ranges with valleys to the north, with mountains that reach elevations greater than 3500 m ASL south of the Bishkek site and 4600 m ASL south of the LST site, and essentially no population to the south. At each site, $PM_{2.5}$ mass was measured continuously with tapered element oscillating microbalance (TEOM) instruments and $PM_{2.5}$, PM_{10}, BC, and OC were obtained using filter-based sampling with samples collected for 24 h every other day. AOD was measured every day at 10:30 am local time (LT) using Microtops-II sun-photometers (SP). A stationary three wavelength aerosol Lidar measured vertical profiles of extinction and depolarization on an event basis at the LST site. The Lidar vertical profiles provide information on vertical distribution of the particles, and were also used to calculate AOD from the Lidar Extinction (LE) profiles and to estimate the height of the planetary boundary layer (PBL) as described in Chen et al., (2013). These observations sites are now part of the UNEP project ABC measurement network (http://www.rrcap.ait.asia/abc/index.cfm). Further details of the study can be found in Miller-Schulze et al., (2011). Observations from these sites were obtained for the period April 2008 to July 2009 (the TEOM measurements were available from April 2008 and filter measurements began from July 1, 2008).

The Moderate Resolution Imaging Spectroradiometer (MODIS) collection 5.1 Level 2 AOD products (~ 10 km horizontal resolution) at 550 nm wavelength from Terra and Aqua satellites were used to compare the observed and simulated AOD. The MODIS Level 2 data were used and included land and ocean AOD retrieved via the dark target algorithm (Remer et al., 2005, Levy et al., 2007), and the Deep Blue AOD over land (Hsu et al., 2004, Hsu et al., 2006), which can retrieve AOD over bright and desert surfaces. This is particularly relevant for the CA region, which contains major dust sources in western China, South Asia, the Middle East, and Africa (Ginoux et al., 2001). The MODIS Level 2 to Level 3 averaging procedure outlined in Hubanks et al., (2008) was employed to interpolate the 10 km Level 2 AOD products to the 60 km horizontal model resolution on a daily basis. Level 2 QA flag weightings were used to reduce the uncertainty associated with the MODIS retrievals. In grid cells where both the MODIS dark target and Deep Blue AOD were retrieved, the mean value of the two was used.

2.2. Modeling System

2.2.1 Meteorological Model

The Weather Research and Forecasting (WRF) model (Skamarock et al., 2008) version 3.2 was used to generate the meteorological fields needed for simulating the transport patterns in the STEM model (D'Allura et al., 2011). The WRF simulations for each day were initialized using the meteorological boundary conditions obtained from National Centers for Environmental Prediction (NCEP) Final Analysis (FNL, http://rda.ucar.edu/datasets/ds083.2/). A daily 24 hour spin up time for WRF was used (i.e. WRF was run for 48 hours each day and the first 24 hours were treated as spin up and were discarded). The STEM model simulation time period was from April 2008 to July 2009.

153 2.2.2 Chemical Transport Model

154 The STEM model (Carmichael et al., 2009) was used to simulate the mass of sulfate, BC,
155 OC, other primary emitted $PM_{2.5}$, and other primary emitted PM_{10} (i.e., non-carbonaceous PM
156 such as fly ash, road dust, and cement), which were simulated as a single mass component with
157 aerodynamic diameters less than or equal 2.5 μm, and between 2.5 and 10 μm (denoted as coarse
158 fraction), respectively and referred to in this paper as $OPM_{2.5}$ and OPM_{10}, dust (fine and coarse)
159 and sea salt (fine and coarse). Nitrate and secondary organic aerosols (SOA) were not included in
160 the model for this application. The nitrate aerosol is estimated to be a minor component of the
161 PM mass in CA (Baurer et al., 2007). The importance of SOA will be discussed later in the
162 paper. The dry deposition of aerosols was modeled using the "Resistance in Series
163 Parameterization" (Wesely and Hicks, 2000) and wet deposition was calculated as a loss rate
164 based on the hourly precipitation calculated from the WRF model. Further details of the wet
165 scavenging can be found in Adhikary et al., (2007). The modeled AOD at 550 nm wavelength
166 was calculated using the simulated three dimensional aerosol distributions and species specific
167 extinction coefficients as described in Chung et al., (2010).

168 2.2.3 Modeling Domain

169 The STEM and WRF computation domains were identical, with a 60 ×60 km horizontal
170 resolution (249 ×249 horizontal grid cells) and 22 vertical layers up to 10 hPa. The domain (Fig.
171 1) covered much of the northern hemisphere in a polar stereographic projection, centered over
172 the Arctic region and extended to 35° N to include the major emission regions of North America,
173 Europe, and Asia. This modeling system has been applied to simulate aerosol distributions in
174 several field campaigns as described in D'Allura et al., (2011) and further details describing the

model can be found there. STEM was initialized with a one month spin up using March 2008. Much of the analysis for this paper is focused on the domain denoted by the rectangle centered over CA shown in Fig. 1. This domain has large gradients in topography (insert Fig. 1), which significantly impact the transport patterns in the region.

2.2.4 Air Mass Trajectories

The CA observation sites are impacted by dust, anthropogenic pollution, and biomass burning emissions from various source regions. To further understand the transport pathways and source region influences on the PM distributions at these sites, three dimensional ten day air mass trajectories (both forward and backward in time) from each site were calculated for the entire time period (April 2008 – July 2009). In this trajectory analysis, we utilized the three dimensional wind fields (including u, v and w components) along with the above ground level (AGL) altitude simulated by the WRF meteorological model consistent with Dallura et al., 2011 study. These trajectories describe the general flow patterns based on wind fields alone and provide useful information about the history of air mass particularly the influence of source regions over which the air mass had resided before arriving at the site of interest. Note that these trajectories do not account for any other atmospheric processes such as diffusion or chemical evolution along its path (Kurata et al, 2004 and Guttikunda et al., 2005).

To understand the differences in transport patterns at the surface and aloft, and to study the impact of topographic gradients in the vicinity of the sites, trajectories were initialized at different altitudes (0.1 (100m), 0.3 (300m) 0.5 (500m), 1, 2, 3, and 5 km) a.g.l at the site locations (i.e. latitude and longitude) daily every 3 hours for a ten day period both backward and

forward in time. The trajectories were terminated when they touched the ground, or went out of the model domain or exceeded the ten day calculation period. The trajectories (at or below 1 km) were used to characterize transport pathways impacting the surface concentrations at these sites, which are discussed later in section 3.5.

2.3. Emissions

2.3.1 Base emissions

Anthropogenic emissions of BC, OC, $PM_{2.5}$, PM_{10}, and SO_2 were based on the ARCTAS emissions described in D'Allura et al., (2011), but updated with newly available information. For India and China BC, OC, and SO_2 emissions from Lu et al., (2011) were utilized, and INTEX-B emissions were used for the rest of Asia (Zhang et al., 2009). For Europe, the EMEP 2008 (http://www.ceip.at/webdab-emission-database/officially-reported-emission-data) emissions were used for SO_2, $PM_{2.5}$, and PM_{10}, and the EUCAARI 2005 inventory was used for the carbonaceous particles (BC and OC) (Visschedijk et al. 2009 and Denier van der Gon et al. 2009). The shipping emissions came from the IIASA base year 2005 inventory (UNEP and WMO, 2011). Mass conservative regrinding tools including MTXCALC and MTXCPLE from the IOAPI m3tools suite (http://www.baronams.com/products/ioapi/AA.html#tools) were used to interpolate the input raw emissions described above on to the model grid.

Anthropogenic emissions for SO_2, BC and OC were available by major economic sectors; i.e., transportation, residential, industry, and power. The industry and power sectors were treated as small and large point sources, respectively, and emitted into the first 6 model levels (lowest 2 km). The residential and transportation emissions were treated as area sources and partitioned into the first two model levels with a 90 – 10 percent split. Monthly emission allocation factors

were applied over India and China for the economic sectors from Lu et al., (2011). The rest of the domain (i.e. excluding India and China) used same emission rates for all months due to unavailability of monthly emission allocation factors.

The Fire Inventory from NCAR (FINN v1) was used for BC, OC, CO, SO_2, $PM_{2.5}$ and PM_{10} biomass burning emissions from forest, grassland and crop residual fires. The FINN database, which is based on MODIS fire detection as thermal anomalies, provides global coverage of fire emissions at a spatial resolution of ~ 1km on a daily timescale (Wiedinmyer et al., 2011). The WRF-Chem fire utility (http://bai.acd.ucar.edu/Data/fire/) was employed to interpolate the speciated FINN emissions to the WRF model grid. The gridded two-dimensional FINN emissions were used as input to the WRF-Chem (Grell et al., 2005) plume rise model (Grell et al., 2011), which implements the Freitas et al., (2007) and Freitas et al., (2010) algorithm to compute injection heights and to calculate the vertical distribution of fire emissions at an hourly time step, which were further utilized as input to STEM model simulations.

Sea salt and dust emissions were calculated using the WRF meteorological fields based on the methods described in Gong, (2003) and Uno et al., (2004), respectively. The dust emissions were further constrained with snow cover (SNOWC variable from WRF output) and only grid cells with snow cover < 1% were used for dust emission calculations.

Fig. 2 shows the annual gridded anthropogenic SO_2 and BC, dust, and biomass burning $PM_{2.5}$ emissions in Gg per grid in and around CA. Large BC emission hotspots can be seen over the Indo-Gangetic plain and eastern China. Significant BC emissions are also seen over Europe, but are relatively lower in intensity than the Asian sources. The SO_2 emissions show Eastern China as the largest source region followed by regions of South Asia, Europe, and Russia. The

major natural dust emission sources (Fig. 2c) include Africa, the Middle East, CA, Western India boundaries, and Western China. The major sources of biomass burning are Eastern Europe, portions of Siberian (between 40 – 60° N), Southeast Asia, Southern China and India (Fig. 2d).

Dust emissions have a strong seasonal cycle. The major dust sources in the region (Fig. 1) are located to the east, west and south of the observation sites and include the cool winter deserts around the Aral and Caspian seas and those in western China and northern Pakistan as well as the sub-tropical deserts in western India, around the Persian Gulf and northern Africa. The emissions from the cool winter deserts occur when the surfaces are free of snow cover (from March through October). Emissions from the sub-tropical deserts can occur throughout the year.

The open biomass burning emissions that impact CA also have a strong seasonality with minimum impact in winter (Supplemental Materials Fig. S1). Fires typically begin in the spring in Siberia along 50° N latitude and in northern India and South East Asia and in summer the high latitude burning shifts to the west. In October the fire activity decreases and remains low until spring, with the most active fire regions associated with agricultural burning in northern India and southeast China.

2.3.2 Future Emissions Scenarios

In addition to the base emissions, a series of simulations were analyzed using emission scenarios for 2030. These scenarios were developed for the WMO/UNEP report that looked at short lived climate pollutants as described in Shindell et al., (2012) and Anenberg et al., (2012). The reference scenario for 2030 was based on the implementation of control measures currently approved in the various regions and assumed their perfect implementation. The 2030 reference

scenarios were developed from a reference global emissions inventory with a 2005 reference year, and assumed significant growth in fossil fuel use relative to 2005, leading to increases in estimated CO_2 emissions (45%). Abatement measures prescribed in current legislation were projected to lead to reductions in air pollutant emissions, which varied by pollutant and region. In the 2030 reference scenario, total primary $PM_{2.5}$ emissions remain approximately constant, while BC and OC decline by a few percent. However, in the study domain emission changes varied widely. BC emissions increased by 10 – 100% in CA, South and Southeast Asia and in western China, and decreased in East Asia and Europe. The $PM_{2.5}$ emissions showed similar regional changes but grew at smaller rates (10 – 40%). SO_2 emissions generally increased throughout the region by 10 – 20%. Spatial maps of emission changes for the 2030 reference scenario are presented in Figs. S2b, S3b, and S4b.

A series of emission control scenarios for 2030 were developed to evaluate the impact of additional abatement measures designed to reduce the levels of short lived climate pollutants (e.g., BC). The BC measures in the scenarios included two different sets of assumptions (low and lowest). The first focused on reductions from incomplete combustion sources. These included implementation of Euro 6 equivalent vehicle emission standards (requiring installation of diesel particulate filters) and improving traditional biomass cook stoves in developing countries (assuming 25% decrease in BC and 80 – 90% decreases in OC, CO, non-methane volatile organic compounds(NMVOC), methane, and direct $PM_{2.5}$, relative to emissions from traditional stoves). Under this scenario BC and $PM_{2.5}$ emissions in the study region are projected to decrease throughout most of the domain, with SO_2 emissions showing almost no change (see Figs. S2c, S3c, and S4c).

288 The lowest option assumed the additional elimination of high-emitting vehicles, biomass
289 cook stoves (in developing countries), and agricultural waste burning. These BC measures in the
290 lowest scenario reduced global anthropogenic BC emissions by 75%. Measures targeting BC
291 also substantially reduced total primary $PM_{2.5}$ (-50%), OC (-79%), NO_x (-27%), and CO (-44%).
292 These BC measures have little impact on SO_2 emissions. Projected emissions of BC and OC
293 under these scenarios are reduced most in Asia, followed by Africa. North America, and Europe.

294 These measures were also combined with a scenario designed to stabilize greenhouse
295 gases at 450 ppm of CO_2 equivalent (lowest+450ppm scenario), consistent with a global average
296 temperature increase of ~2° C. These CO_2 measures reduced SO_2 (-30%) (Fig. S4d) and NO_x (-
297 20%), but had little further impact on BC (~5% decline, Fig. S2d) since the major sources of CO_2
298 differ from those of BC. $PM_{2.5}$ emissions were substantially further reduced under this scenario
299 (Fig. S3d).

300 **2.4. Simulations Analyzed**

301 Several simulations were analyzed for this paper. The *base* simulation included all
302 sources and used the meteorology from the WRF model for the period April 2008 – July 2009.
303 To investigate the contributions from specific source sectors, additional simulations were
304 performed where emissions from one sector were set to zero everywhere. The contribution from
305 each sector was calculated as the difference between the base simulation and the simulation with
306 emissions from that particular sector set to zero. This was repeated for each sector and for
307 biomass burning. Additional simulations were performed to assess the source contribution from
308 specific regions to the particle levels in CA. The specific regions used are shown in Fig.1. In
309 these simulations all anthropogenic emissions were set to zero in that region. In a similar manner

regional dust and fire sources were also studied and the source regions are also shown in Fig.1. Finally, simulations were performed using the *reference* 2005 and 2030 emissions and the *low* and *lowest + 450 CO_2* 2030 scenarios (described above). For these runs, the meteorology, open biomass burning, and dust emissions were the same as in the base run (i.e., 2008/2009).

3. Results and Discussion

3.1. Regional Perspective

CA is a region with high aerosol loadings as shown in the mean MODIS retrieved AOD at 550 nm for the time period of study (April 2008 – July 2009) (Fig. 3).AOD (period mean) throughout CA (~ 45-90° E, 35-50° N) are greater than 0.25, with the highest regional values around the desert areas near the Caspian and the Aral seas. There are also high values (>0.6) along CA's eastern border, which reflect the deserts and rapidly developing cities in western China, and to the south over Pakistan and northern India.

The predicted period mean AOD spatial distribution shown in Fig. 4d captures the main observed features. The period-mean predicted surface concentrations of $PM_{2.5}$, BC, and total dust (fine and coarse) are also plotted. The period mean $PM_{2.5}$ concentrations in CA (10 to 35$\mu g/m^3$) have a similar geographical distribution as AOD. Dust is the major component of predicted PM_{10} in CA and concentrations are high (25-100 $\mu g/m^3$). The BC levels in CA are typically less than 0.3 $\mu g/m^3$ and its spatial pattern reflects contributions from both anthropogenic and biomass burning sources.

3.2 Comparison with surface observations in CA

331 The surface observations at the two CA sites provide the opportunity for the first time to
332 evaluate the performance of chemical transport models in estimating the distribution of aerosols
333 in CA and to assess the emission estimates in the region. A comparison of the predicted and
334 observed meteorology is presented in Fig. 5, where the distributions of key meteorological
335 parameters for the entire measurement period are shown as box-plots. The model accurately
336 predicted the magnitude and variability in temperature and relative humidity. For example the
337 model mean value of temperature and relative humidity are 279.3K and 61.6% in comparison to
338 the observed values of 280.3K and 59.2% at the LST site. The model wind speeds were biased
339 high by about 30% (mostly in winter, see section 3.4) and the direction had a southwest bias.
340 These biases are due in part to the 60 km model grid size, which is too coarse to capture the steep
341 gradients in topography in and around the observation sites, and to the site placement in small N-
342 S oriented valleys. More details regarding the evaluation of the modeled meteorology can be
343 found in the Supplemental Materials, Table S1.

344 The observed and modeled distributions of AOD and PM are compared in Fig. 6. The
345 AOD observations based on the LE on average are ~50% larger than those from the SP. Modeled
346 AOD on average are ~20-30% higher when compared to SP at the Bishkek and LST sites and ~1
347 % lower when compared to the LE values. The variability in the predictions is slightly under-
348 estimated. $PM_{2.5}$ is over predicted (~50%) and the spread is accurately captured, while PM_{10} is
349 over predicted by ~70%. This leads to an underestimation of the $PM_{2.5}/PM_{10}$ (0.4 predicted
350 versus 0.5 observed) and also helps account for the overestimation in modeled AOD (by ~20-
351 30%).

352 Chemical analysis of the filter and soil samples in the CA dust regions have been used to
353 estimate the dust contribution to measured PM at the two sites and to help identify source regions
354 of importance (Park et al., 2014). The emission regions within CA, including around the Aral
355 Sea, and western China were identified as the most important dust sources, which is consistent
356 with the regions identified in the simulations. Dust was estimated to comprise between 5-40% of
357 $PM_{2.5}$ mass at the LST site and to vary by season (minimum values in winter). The observation-
358 based estimates of dust percentage contribution suggest that modeled dust is over predicted by
359 ~2 times. Thus it appears that dust is a main reason for the over prediction of $PM_{2.5}$ and PM_{10},
360 and that dust emission models need to be refined for CA applications.

361 The overestimation in PM mass at the surface could also be impacted by errors in the
362 modeled PBL heights. The PBL height as determined by the Lidar aerosol profiles varies
363 seasonally and is highest in the summer (from 2-4 km AGL) and lowest in the winter (Nov-Feb,
364 0.5-1.5 km AGL) (Fig. S5). The predicted PBL heights show a similar seasonal cycle with a
365 tendency to under-predict the heights in all seasons as indicated by the comparison of the
366 distributions of the observed and predicted values (Fig. 5), and this occurs in all seasons (Fig
367 S5). The lower PBL height in the model contributes a systematic high bias in surface
368 concentrations driven by near surface emissions. Further statistical details of the model-
369 observation comparison can be found in the supplemental materials (Tables SM2 & 3). The
370 seasonal variability in the observations is discussed in further detail later (section 3.4).

371 We have evaluated this model framework in other regions outside CA including arctic
372 region and continental US, which are summarized below. Dallura et. al., 2011 evaluated the
373 performance of the WRF-STEM modeling framework (used in this study) through the case study

of the ARCTAS mission DC-8 flight conducted on July 9 2008. The WRF model compared well with observed meteorological variables (including temperature, pressure, wind speed and wind direction) along the flight and correctly simulated the various meteorological processes (i.e. cyclonic circulation, low pressure system, anticyclones and geostrophic wind flows) that facilitate transport of pollutants into the Arctic region. This study also compared CO along the flight and found that the simulated values were able to capture the magnitude and temporal variability seen in observed values. The study also found that the fires from North Asia and anthropogenic CO from China were the major sources contributing to observed CO levels along the flight suggesting that the midlatitude pollution and summertime forest fires/biomass burning transport events were well represented in the STEM model.

The study by Huang et al., 2012 used the STEM model to simulate summertime sectoral and regional contributions to BC over continental US and evaluated the model performance aloft and at surface using measurements from ARCTAS mission DC8 flights conducted on June 20 and 22 and 24 that sampled over California and Interagency Monitoring of Protected Visual Environments (IMPROVE) surface site network. Huang et al., 2012 found that the predicted BC values captured many of the vertical features seen in the flight observations with a tendency to over predict surface BC and > 4km. The comparison of predicted BC with observed values from IMPROVE network showed that the model was able to capture the gradients in BC values with high concentrations in western and eastern NA regions with slight positive and negative biases over the mountain regions and the eastern US and CA.

Since the Huang et al., 2012 study was focused on summer, we evaluated the simulated BC values with IMPROVE BC observations for the simulation time period (i.e. April 2008 –

July 2009) used in this study. The IMPROVE BC analysis is limited to 27 sites on the US west coast (i.e. west of 120 W) to be consistent with the focus of this paper (i.e., long range transport of pollutants on a hemispheric scale). The mean observed and modeled BC for the West Coast sites are ~0.16 and 0.19 μg m−3 (n = 3759 points) with mean bias and RMSE of 0.03 μg m−3and ~ 32 % respectively. The mean simulated/observed BC at surface sites is ~ 1.2, which compares well with the corresponding ratio of 1.6 reported in the global model performance over North America region by Koch et al., 2009. The detailed analysis of the IMPROVE BC sites and associated seasonality will be the addressed in a future paper.

These studies indicate that the simulated transport patterns are able to capture the main important features of the hemispheric flows at the scale discussed here for improving the current understanding of the source receptor relationships of aerosols at intercontinental scales. The prediction of aerosol mass and composition at the hemispheric scales is also quite good, but has considerably higher uncertainties associated with emission estimates (in particular forest fires/biomass burning and natural dust emissions) and wet removal processes (Bates et al., 2006).

3.3 Source Contributions to $PM_{2.5}$

Model simulations were performed to identify the component, source region and emission sector contributions to $PM_{2.5}$ mass. Period means for the spatial average over the entire CA region (see Fig. 1) and for the grid cells for the Bishkek and LST observation locations are presented in Fig.7, and their comparison provides insights into the spatial variability of PM and its sources within CA, and how representative the observation sites are at characterizing CA PM. The component contribution to AOD at the sites and for the CA average are similar, with the major contributions coming from fine dust, sulfate, and OC. Spatial maps of mean percent

418 contributions of the various components (i.e., BC, OC, sulfate, OPM, dust and sea salt) to AOD
419 and $PM_{2.5}$ mass are presented in Figs. S6 & S7, respectively. Coarse particles contribute ~10% to
420 mean AOD. Dust accounts for >60% of the calculated $PM_{2.5}$ mass at the observation sites and for
421 the CA region. The dust source regions (see Fig. 1) contributing to $PM_{2.5}$ vary within CA. Dust
422 from the CA source regions has the largest influence on the region mean dust- $PM_{2.5}$ mass. At the
423 LST site, which is located in the far east of CA, western China dust sources have their largest
424 influence (~40%). African and Middle East source regions have their largest influence on the
425 Bishkek site (20 and 15%, respectively), and collectively contribute ~25% to regional CA dust
426 $PM_{2.5}$.

427 The source region contributions to the non-dust $PM_{2.5}$ are very similar for the Bishkek
428 and LST sites, with CA sources making the largest contribution (~50%) followed by Europe
429 (~20%), the Middle East (~15%), and biomass burning (~15% from all sources). For the entire
430 CA region the European source contribution is as large as the CA sources (~30% each), with
431 larger contributions from biomass burning and Russia sources and smaller contributions from
432 Middle East emissions than at the observation sites. The significant contribution from Europe
433 sources reflects their large anthropogenic emissions and the general westerly transport patterns.
434 On average the impact from South Asia sources are small. North America sources contribute
435 between 3 to 7% to $PM_{2.5}$ in CA. Of the biomass burning contribution to $PM_{2.5}$, the Siberian and
436 European fires (see Fig. 1 for fire regions) contribute 63 and 25%, respectively, with
437 contributions from South/Southeast Asia and North America fires each contributing ~5%. The
438 power and industrial sectors are identified by the simulations as the largest contributors (~40%
439 each) to non-dust $PM_{2.5}$ mass in CA.

3.4. Seasonal Variations in AOD and PM at the Observation Sites

AOD has a seasonal cycle with the lowest values in winter and highest values in spring and summer as shown in Fig. 8 by the AOD observations at the LST site from both the SP and the LE profiles. A similar seasonal cycle was observed at the Bishkek site (not shown) and in the MODIS AOD retrievals (Fig. S8). The modeled AOD captures this seasonal variation, with a tendency to over predict the values during the periods with the lowest observed AOD.

The seasonal cycles in $PM_{2.5}$ (Fig. 9) and PM_{10} are similar to those for AOD, with minimum values in October – February. At the LST site $PM_{2.5}$ from both the filter based and the non-volatile TEOM measurements are plotted. Both the observations and the model find a strong similarity in the time series at the two sites.

There is also a clear seasonality in the surface meteorology in the region as shown by the time series in surface temperature and relative humidity at the two sites (Fig. 10). There are distinct temperature minima in the winter and relative humidity minima in the summer. However there is not a clear seasonality in wind speed and direction, and the winds are generally from the south and less than 4m/s throughout the year at the LST site (not shown).

The source region and component contributions exhibit seasonal variability as shown by the modeled contributions to $PM_{2.5}$ mass in Fig. 11. Dust is found to be the main driver of the seasonal cycle of $PM_{2.5}$. The dust contribution to $PM_{2.5}$ is peak in spring and minimum in winter (<20%). During this time period the transport of air masses to the sites are from the west and the southwest. When the transport is from the east then dust sources from western China can impact

461 the stations. This transport pattern occurs episodically throughout the year, with contributions
462 from western China sources as large as 20 to 50%. The dust seasonal cycle is in turn influenced
463 by the seasonal variations in meteorology that drives the dust emissions and transport. The
464 seasonal changes in the dust source regions can be seen in the seasonal spatial maps of AOD
465 (Fig. S8). Throughout the domain, AOD in the dust regions are highest in March – October and
466 lowest in winter (Fig. S8) as the nearby dessert regions are snow covered.

467 Biomass burning also adds to the seasonal cycle, and its contribution is minimum in the
468 winter. South Asia sources can impact the sites in the winter time. The periods when North
469 America sources impact the site are associated with strong transport events across the Atlantic
470 and subsequent subsidence towards the surface associated with high pressure systems as they
471 move towards CA. The transport pathways are discussed in more detail in Sect. 3.7.

472 **3.5 Source Contributions to BC**

473 Because of its dual role as an air pollutant and as a climate warming agent there is special
474 interest in understanding the regional and sector contributions to BC (Ramanathan and
475 Carmichael, et al., 2008). BC comprises on average only about 1-2% of $PM_{2.5}$ mass in CA. The
476 period mean predicted BC surface concentrations are ~0.1 $\mu g/m^3$ at the two observation sites and
477 0.15 $\mu g/m^3$ for the CA regional average. As shown in Fig. 7, European emissions contribute
478 ~50% to the mean BC concentrations in CA, while Middle-eastern and biomass burning sources
479 each contribute ~15-20%. Residential and transport are the most important sectors each
480 contributing ~30% to BC in CA, followed by industry (~20%), and with power the least
481 important. This is in contrast to the sector contributions to non-dust $PM_{2.5}$ mass, where power
482 and industry are the most important sectors. On average biomass burning contributes ~10% to

483 BC mass, with Siberian and European fires accounting for 61% and 33%, respectively. The
484 source contributions to OC are shown in Fig. S9.

485 There is also large seasonal variability in BC concentrations and source sector/region
486 contributions (Fig. 12). BC surface concentrations show the highest values in fall/winter (as do
487 the observations), when there is maximum contribution from the residential sector, reflecting the
488 wide-spread use of biofuels and coal for heating in the region. The source region contributions
489 vary by season, with maximum contributions from Europe and China. South Asia sources
490 contribute in the winter. Biomass burning also is an important source of BC and plays an
491 important role in influencing daily and seasonal variability in BC concentrations.

492 Predicted BC captures the seasonality and the magnitude of the spring and summer
493 values as observed, but concentrations are biased low in the fall/winter. Median BC
494 concentrations (and variability) are underestimated by a factor of 2 at both observation sites (Fig.
495 6 and Tables S2&3)). The high wind speed bias in winter (~ factor of 2), should result in too
496 rapid dispersion and could contribute to the negative bias, but the negative bias in the PBL
497 heights should lead to higher predicted concentrations. Thus this negative bias is likely related to
498 emissions (an indication of an underestimation of the heating fuel use).

499 The OC concentrations follow a similar seasonal cycle as BC and are also under
500 predicted (Fig. 6 and Tables S2 & 3)). Furthermore the OC/BC ratio is under predicted by a
501 factor of ~3 (Fig. 6). The observed OC/BC ratio follows a seasonal cycle with values >15 in
502 summer and ~5 in September through April. Part of this under prediction in OC and the OC/BC
503 ratio is due to the fact that SOA is not estimated in the model. However a source contribution of
504 OC using the filter data and chemical mass balance (CMB) approach found that SOA sources

were very low in winter and only ~ 20% in summer (Miller-Schulze et al., 2011). Thus SOA cannot account for the model under prediction of winter values. There appears to be an underestimation of regional OC primary emissions. SOA can however help account for the large values of OC/BC observed in the summer and not predicted.

Biomass burning emissions cannot account for the underestimation in winter BC and OC. The largest impact of fires at the observation sites is in the late summer, when the fires are concentrated in western Russia and the wind direction is such that the smoke is transported into CA. Fires from South Asia can impact the sites associated with the fires and high pollution levels in northern India and with winds from the south, which can occur in late fall, but not frequently.

The fact that BC and OC are systematically under predicted in the winter suggests that local/regional emissions during the heating season may be underestimated. This is supported by the results of the CMB analysis of OC discussed above that found the contribution from biofuel combustion increased 2-3 times in the fall and winter periods. The uncertainty in emissions can also be partly caused by the lack of seasonal emissions over this region as described earlier in section 2.

3.6 Vertical Distributions

Figure 13 shows the predicted weekly averaged vertical distributions of $PM_{2.5}$, dust, and BC for the entire simulation period at the LST site. These plots show more clearly that much of the variability in the PM loadings is associated with dust and biomass burning episodes (as represented by the enhancements in BC). Typically the high PM episodes show elevated PM

mass that extend from the surface to 2 to 4 km. The vertical extents show a seasonality associated with seasonal variations in the PBL heights. These vertical distributions indicate that much of the transport of aerosols in CA occurs via low altitude pathways. In some cases there are large amounts of dust and biomass burning aerosol in the 3-6 km altitude range that are decoupled from the surface (e.g., dust in early May 2009), reflecting that some aerosols are lifted out of the boundary layer and are transported at high altitude over CA, enhancing AOD but not contributing to ground-level mass concentrations at the observation sites. These vertical features are confirmed by the aerosol extinction profiles observed at the LST site as discussed in Chen et al., (2012 b). The variation in weekly averaged AOD can be significant (Fig. 13 bottom panel) and is driven by variations in dust and biomass burning emissions.

3.7 Transport Pathways

The three dimensional ten day air mass trajectories (described in section 2.2) were utilized to further understand the transport pathways of air masses entering into and exiting out of the CA region and its subsequent impact of source regions on the aerosol distributions at the CA sites.

3.7.1 Transport into CA

The air mass transport into CA is discussed through back trajectories associated with the five events labeled on Fig. 13. These five events represent transport episodes with elevated surface $PM_{2.5}$ (averaged over the three hour time window consistent with trajectory time step) with varying contributions from biomass burning, anthropogenic pollution, and dust sources. In

each trajectory figure (Figs. 14 and 15), the regions with active dust (blue diamond hatches) and biomass burning emissions (green square hatches) for the event time period and prior ten days are identified and MODIS AOD (values printed in black) overlaid. The trajectories are color coded by region to distinguish the source impacts. The regions include: Africa (blue), Middle East (green), CA (yellow), North Asia biomass (> 50° N, black), Europe (brown), China (red) and South Asia (orange).

Figure 14 shows the first two events for August 2008. The first event in early August (Fig. 13, event labeled 1) is a high dust event associated with trajectories from the west passing over the dust regions of the Aral Sea (~45N, 55E) and eastern trajectories passing over the Taklimakan region of western China (90-100E, 40N). These were both regions with active dust emissions as indicated by the elevated MODIS AOD values. Thus the PM increases during this event were due largely to dust emitted from CA and western China deserts. The second event in the latter half of August is characterized by high levels of BC without dust. During this episode the transport to the site was under the influence of a high pressure system located to the northwest and air masses were transported over the active fire region in western Russia.

Figure 15 shows winter and spring events. The November episode (event 3) is a period with elevated BC and $PM_{2.5}$ from pollution sources from South Asia (including some fires) and western China and low fire and dust emission activity. The January episode (event 4) is a period of elevated BC with air masses coming from Europe, indicating the influence of anthropogenic pollution coming from this industrialized region, and from CA sources. Dust emissions from CA and Africa were low during this period. The final illustrative episode is for April 2009 (event 5),

568 a period with both elevated levels of dust from western China, CA and Africa and BC from both
569 fire and anthropogenic pollution from Europe, CA and Russia sources.

570 These examples provide insights into the source region contributions to PM mass in CA
571 as presented in Figs. 11 & 12). CA is an ideal location to observe a variety of source regions as it
572 is at the crossroad of transport patterns with air masses impacted from dust, anthropogenic
573 activity and biomass burning from different geographical regions.

574 3.7.2 Long range transport of CA sources

575 The transport pathways out of CA were also evaluated by calculating forward trajectories
576 from the observation sites. Selected forward trajectories initialized at or below 1 km are used to
577 represent the transport of boundary layer PM from CA and these are shown for summer, winter
578 and spring periods in Fig. 16. In these plots the MODIS AOD, dust, and fire emissions plotted
579 for each event represent values averaged over the subsequent ten days and trajectories were
580 stopped if they impacted the surface. During the summer, outflow from CA is towards the north
581 in association with the summer monsoon system. Figure 16a shows the subset of forward
582 trajectories that reside for at least 3 days over the region 48 - 65° N during June 2008.
583 Trajectories typically pass over Russia and reach into the Arctic and also can be caught in
584 westerly storm tracks and reach the higher latitudes of the northern hemisphere. During the
585 winter, air mass transport out of CA is associated with the winter monsoon system and the
586 transport pathway is over Mongolia and then over eastern China as seen in Fig. 16b. In this
587 figure, forward trajectories that pass over the region west of 130° E during late December 2008
588 are shown. Figure 16c illustrates transpacific transport of CA air masses. Plotted are the forward
589 trajectories that stay within the 30 – 50° N region for at least 3 days during the month of April

2009. During the spring transport from CA is dominated by strong westerly flows and air masses are transported over China, Korea, and Japan and then across the Pacific, reaching North America in 7 – 10 days.

PM arising from dust and anthropogenic emissions from CA impact the entire northern hemisphere as illustrated in the hemispheric maps of seasonal average surface dust concentrations due to CA emissions only (Fig. 17). The predominant westerly flows in all seasons in the northern hemisphere result in the bulk of the CA emissions being transported to the west. The contribution of CA sources to surface PM concentrations of 0.35 $\mu g/m^3$ or greater covers large portions of the northern hemisphere, including the Arctic, all of Asia, much of Europe, and portions of the continental US.

There are episodic and seasonal components to the intercontinental transport as shown in the time series of the vertical profiles of $PM_{2.5}$ at Mt. Bachelor, Oregon (43.97N, 121.69W, 2700m agl) (Fig. 18). The bulk of the CA particle transport takes place in the free troposphere and impacts surface concentrations in the US as the boundary layer grows and entrains "plumes" aloft. This occurs most frequently in spring, summer and fall. The episodic contributions of CA sources to surface concentrations can exceed 1.5$\mu g/m^3$. In the fall, there is also strong transport of dust from CA across Europe and out into the Atlantic.

3.8 Future Scenarios

How might PM levels change in CA over the next few decades? To address this question, simulations were repeated for various emission scenarios developed and used in the

611 WMO/UNEP assessment on short-lived climate pollutants (Shindell et al., 2012) as described in
612 Sect. 2. Dust and biomass burning emissions and meteorology were the same as those used in the
613 2008/2009 simulations. The period mean changes in surface BC and $PM_{2.5}$ concentrations in
614 2030 for the reference scenario are shown in Fig. 19a, d, respectively. This scenario reflects all
615 present agreed policies affecting emissions and assumes that they are fully implemented. Under
616 this scenario $PM_{2.5}$ increases significantly in South Asia and western China (>50%) and in parts
617 of CA, including the area where the sampling sites are located. $PM_{2.5}$ decreases in Western
618 Europe and Eastern China (< 10%). BC surface concentrations show a similar pattern to $PM_{2.5}$,
619 although covering larger portions of CA with relatively larger increases in BC than in $PM_{2.5}$.
620 These results suggest that health impacts and climate warming due to BC and $PM_{2.5}$ may increase
621 in coming decades unless additional emission control measures are implemented.

622 Results for two other scenarios are also presented in Fig. 19. One scenario specifically
623 targets BC emission reductions in recognition that BC is also a major contributor to atmospheric
624 warming (Ramanathan and Carmichael, 2008). These additional measures significantly reduce
625 2030 BC concentrations by greater than 35% throughout most of the domain, with only a few
626 regions (e.g., Myanmar and eastern Afghanistan) showing increases in BC relative to 2005
627 levels. This scenario assumes that all BC emission reduction measures are perfectly implemented
628 and 100% effective. BC measures also impact emissions of co-emitted pollutants (e.g., OC and
629 SO_2). $PM_{2.5}$ concentrations under this scenario (Fig. 19e) are reduced, but by much smaller
630 amounts, and concentrations still increase relative to 2005 over large regions of South Asia and
631 western China, and parts of CA. These results suggest that health impacts in these regions may
632 increase due to the $PM_{2.5}$ increases whereas positive radiative forcing and health effects due to
633 BC may decrease. When the BC measures are used along with greenhouse gas measures aimed at

keeping CO_2 levels below 450 ppm, the $PM_{2.5}$ levels in South Asia are lower than 2005 levels (Fig. 19f), with few exceptions (one being Myanmar region). This is due to the large decreases in SO_2 and NO_x emissions under this scenario, resulting in significant reductions in particulate nitrate and sulfate (e.g., a ~30% increase in particulate sulfate in CA).

To get a regional perspective of how the future emission changes would specifically impact the CA region (See Fig. 1 for the CA region definition used in this study), we have summarized the changes in emissions and the corresponding concentrations in Table 1.The reference 2030 emissions scenario reports an increase in emissions of BC, SO_2 and $PM_{2.5}$ over Central Asia by ~ 22, 17 and 14 % respectively w.r.t to base 2005 levels. However, the corresponding BC, SO_4 and anthropogenic portion of $PM_{2.5}$ decrease by ~ 5, 12 and 5 % respectively. This suggest that on average the concentration levels go down even though CA emissions increase due to long range transport of pollutants into CA region from the surrounding regions, but locations within CA still increase when dominated by local sources. The Low GWP emission scenario predicts decrease in BC and $PM_{2.5}$ emissions by 31% and 10% respectively with the corresponding decrease in concentrations by ~ 37% and 10 % respectively, while SO_2 emissions remained same as the reference 2030 scenario. The lowest + 450 ppm scenario shows a consistent decreasing trend in emissions and concentration of all the species. This analysis suggests that the impact of the changes in major source region emissions and their subsequent transport to Central Asia will play a major role in determining the future aerosol levels in CA.

4. Summary

AOD in CA during the period April 2008 through July 2009 averaged ~0.3 and displayed a seasonal cycle with the lowest values in the winter and highest values in spring to mid-summer

656 with observed values of AOD > 0.6 and even > 0.8. Surface $PM_{2.5}$ measured at two sites in
657 eastern CA averaged ~10 $\mu g/m^3$ but with large variability (hourly values from 2 - 90 $\mu g/m^3$).
658 Surface concentrations of PM also showed a seasonal cycle with peak values and largest
659 variability in the spring/summer, and lowest values and variability in the winter. BC at these sites
660 averaged ~0.1 $\mu g/m^3$ with peak values (~ 1 $\mu g/m^3$) in the winter.

661 The seasonal cycles and source sector and source region contributions to PM in CA were
662 analyzed using the STEM chemical transport model. Dust was the largest component of the
663 $PM_{2.5}$ and PM_{10} mass in the region in all seasons except winter, whereas sulfate was the largest
664 anthropogenic component of the $PM_{2.5}$ mass. Dust was also found to be the major driver of the
665 seasonal cycles of AOD and PM concentrations. On an annual basis the power and industrial
666 sectors were the most important contributors to $PM_{2.5}$, while residential and transportation were
667 the most important sectors for BC. Open biomass burning within and outside the region also
668 contributed to elevated PM and BC concentrations and to the temporal variability.

669 The model simulations showed a systematic over prediction of PM mass. This is most
670 likely due in large part to the over prediction in dust. Carbonaceous PM was underpredicted and
671 it is speculated that the winter emissions associated with residential heating may be
672 underestimated in the current emissions inventory. The predicted wind speeds were biased high
673 (by ~30%) and the direction had a southwest bias. The high bias in wind speeds may also
674 contribute to the over-prediction in PM_{10}, as dust emissions depend strongly on wind speed.
675 Efforts to improve the dust emissions and to improve the wind speed and direction predictions
676 using a finer model resolution are planned. Additional efforts are needed to improve the
677 anthropogenic emissions estimates for CA.

678 Currently there are few measurements in CA that can be used to quantify the
679 intercontinental transport of pollution from Europe to Asia. The analysis of the transport
680 pathways and variations in PM mass and composition observed at the two sites in CA
681 demonstrate that this region is strategically located to characterize regional and intercontinental
682 transport of pollutants. Aerosols at these sites were shown to reflect dust, biomass burning, and
683 anthropogenic sources from South, East, and CA, Europe, and Russia depending on the time of
684 year. For example, during the spring fine particles from Europe and Africa were transported to
685 CA, on to eastern Asia, and then across the Pacific to North America.

686 Observations of PM and its composition in this region are of growing importance as it is
687 estimated that $PM_{2.5}$ levels are likely to increase significantly in Central and South Asia and
688 western China over the next few decades. Simulations for a reference 2030 emission scenario
689 showed that BC concentrations had a larger relative increase than $PM_{2.5}$ concentrations. This
690 suggests that health impacts and climate warming associated with these pollutants may increase
691 over the next decades unless additional control measures are implemented. Continued pollutant
692 observations in CA will help to characterize the changes that are rapidly taking place in the
693 region.

5. Acknowledgements

The US Environmental Protection Agency through its Office of Research and Development funded this study and collaborated in the research described here as a component of the International Science & Technology Center (ISTC) project # 3715 (Transcontinental Transport of Air Pollution from Central Asia to the US). The University of Iowa activities were also supported in part by the following grants: EPA (RD-83503701-0), NASA (NNX08AH56G), NSF (1049140), NCRR (UL1RR024979) and Fulbright-CONICYT (15093810). Its contents are solely the responsibility of the authors and do not necessarily represent the official views of the funding institutions. This manuscript has been subjected to U.S. EPA review and approved for publication.

6. References

Adhikary, B., Carmichael, G. R., Tang, Y., Leung, L. R., Qian, Y., Schauer, J. J., Stone, E. a., Ramanathan, V. and Ramana, M. V.: Characterization of the seasonal cycle of south Asian aerosols: A regional-scale modeling analysis, J Geophys Res, 112(D22), D22S22, doi:10.1029/2006JD008143 , 2007.

Anenberg, S. C., Schwartz, J., Shindell, D., Amann, M., Faluvegi, G., Klimont, Z., Maenhout, G., Pozzoli, L., van Dingenen, R., Vignati, E., Emberson, L., Muller, N. Z., West, J. J., Williams, M., Demkine, V., Hicks, W. K., Kuylenstierna, J., Raes, F., and Ramanathan, V.: Global air quality and health co-benefits of mitigating near-term climate change through methane and black carbon emission controls, Environ. Health Perspect., 120, 831–839, 2012.

Bates, T. S., Anderson, T. L., Baynard, T., Bond, T., Boucher, O., Carmichael, G., Clarke, A., Erlick, C., Guo, H., Horowitz, L., Howell, S., Kulkarni, S., Maring, H., McComiskey, A., Middlebrook, A., Noone, K., O'Dowd, C. D., Ogren, J., Penner, J., Quinn, P. K., Ravishankara, A. R., Savoie, D. L., Schwartz, S. E., Shinozuka, Y., Tang, Y., Weber, R. J., and Wu, Y.: Aerosol direct radiative effects over the northwest Atlantic, northwest Pacific, and North Indian Oceans: estimates based on in-situ chemical and optical measurements and chemical transport modeling, Atmos. Chem. Phys., 6, 1657-1732, doi:10.5194/acp-6-1657-2006, 2006.

Bauer, S., D. Koch, N. Unger, S. M. Metzger, D. T. Shindell, and D. G. Streets: Nitrate aerosols today and in 2030: a global simulation including aerosols and tropospheric ozone, Atmos. Chem. Phys., 7, 5043–5059, 2007

Carmichael, G. R., Adhikary, B., Kulkarni, S., D'Allura, A., Tang, Y., Streets, D., Zhang, Q., Bond, T. C., Ramanathan, V., Jamroensan, A., and Marrapu, P.: Asian aerosols: current and year 2030 distributions and implications to human health and regional climate change, Environ. Sci. Technol., 43, 5811–5817, 2009.

Chen, B., Sverdlik, L. G., Imashev, S. A., Solomon, P. A., Lantz, J., Schauer, J. J., Shafer, M. M., Artamonova, M. S., and Carmichael, G.: Empirical relationship between particulate matter

and aerosol optical depth over Northern Tien-Shan, Central Asia, Air Quality, Atmosphere & Health, 6.2, 358-396, doi: 10.1007/s11869-012-0192-5, 2012.

Chen, B. B., Imashev, S. A., Sverdlik, L. G., Solomon, P. A., Lantz, J., Schauer, J. J., Shafer, M. M., Artamonova, M. S. and Carmichael, G. R.: Ozone Variations over Central Tien-Shan in Central Asia and Implications for Regional Emissions Reduction Strategies, Aerosol Air Qual Res, 13, 555–562 Available from: 10.4209/aaqr.2012.06.156, 2013.

Chung, C. E., Ramanathan, V., Carmichael, G., Kulkarni, S., Tang, Y., Adhikary, B., Leung, L. R. and Qian, Y.: Anthropogenic aerosol radiative forcing in Asia derived from regional models with atmospheric and aerosol data assimilation, Atmos Chem Phys, 10(13), 6007–6024, doi:10.5194/acp-10-6007-2010, 2010.

D'Allura, A., Kulkarni, S., 5 Carmichael, G. R., Finardi, S., Adhikary, B., Wei, C., Streets, D., Zhang, Q., Pierce, R. B., Al-Saadi, J. A., Diskin, G., Wennberg, P.: Meteorological and air quality forecasting using the WRF–STEM model during the 2008 ARCTAS field campaign, Atmos. Environ., 45, 6901–6910, doi:10.1016/j.atmosenv.2011.02.073, 2011.

Denier van der Gon, H., Visschedijk, A., Droge, R., Mulder, M., Johansson, C., and Klimont, Z.: A high resolution emission inventory of particulate elemental carbon and organic carbon for Europe in 2005, 7th International Conference on Air Quality – Science and Application (Air Quality 2009), Istanbul, 2009.

Emerson, J. W., Hsu, A., Levy, M. A., de Sherbinin, A., Mara, V., Esty, D. C., and Jaiteh, M.: Environmental Performance Index and Pilot Trend Environmental Performance Index, Yale Center for Environmental Law and Policy, New Haven, 2012

Freitas, S. R., Longo, K. M., Chatfield, R., Latham, D., Silva Dias, M. A. F., Andreae, M. O., Prins, E., Santos, J. C., Gielow, R. and Carvalho Jr., J. A.: Including the sub-grid scale plume rise of vegetation fires in low resolution atmospheric transport models, Atmos Chem Phys , 7(13), 3385–3398, doi:10.5194/acp-7-3385-2007 , 2007.

Freitas, S. R., Longo, K. M., Trentmann, J. and Latham, D.: Technical Note: Sensitivity of 1-D smoke plume rise models to the inclusion of environmental wind drag, Atmos Chem Phys, 10(2), 585–594, doi:10.5194/acp-10-585-2010, 2010.

Ginoux, P., Chin, M., Tegen, I., Prospero, J. M., Holben, B., Dubovik, O. and Lin, S.-J.: Sources and distributions of dust aerosols simulated with the GOCART model, J Geophys Res-Atmos, 106(D17), 20255–20273, doi:10.1029/2000JD000053, 2001.

Gong, S. L.: A parameterization of sea-salt aerosol source function for sub- and super-micron particles, Global Biogeochem. Cy. , 17(4), 1097, doi:10.1029/2003GB002079 , 2003.

766 Grell, G. A., Peckham, S. E., Schmitz, R., McKeen, S. A., Frost, G., Skamarock, W. C., and
767 Eder, B.: Fully coupled “online” chemistry within the WRF model, Atmos. Environ. 39, 6957–
768 6975, 2005.

769 Grell, G., Freitas, S. R., Stuefer, M., and Fast, J.: Inclusion of biomass burning in WRF-Chem:
770 impact of wildfires on weather forecasts, Atmos. Chem. Phys., 11, 5289–5303, doi:10.5194/acp-
771 11-5289-2011, 2011.

772 Guttikunda, S., Tang, Y., Carmichael, G., Kurata, G., Pan, L., Streets, D., Woo, J.-H.,
773 Thongboonchoo, N., and Fried, A.: Impacts of Asian megacity emissions on regional air quality
774 during spring 2001, J. Geophys. Res., 110, D20301, doi:10.1029/2004JD004921, 2005.

775 Hsu, N. C., Tsay, S.-C., King, M. D. and Herman, J. R.: Aerosol properties over bright-reflecting
776 source regions, IEEE T Geosci Remote , 42(3), 557–569, doi:10.1109/TGRS.2004.824067,
777 2004.

778 Hsu, N. C., Tsay, S.-C., King, M. D. and Herman, J. R.: Deep Blue Retrievals of Asian Aerosol
779 Properties During ACE-Asia, IEEE T Geosci Remote , 44(11), 3180–3195,
780 doi:10.1109/TGRS.2006.879540, 2006.

781 Huang, M., G. Carmichael, S. Kulkarni, D. Streets, Z. Lu, Q. Zhang, B. Pierce, Y. Kondo, J.
782 Jimenez-Palacios, M. J. Cubison, B. E. Anderson, and A. Wisthaler: Sectoral and geographical
783 contributions to summertime continental United States (CONUS) black carbon spatial
784 distributions, *Atmos. Environ., 51*, 165-174, doi:10.1016/j.atmosenv.2012.01.021,2012

785 HTAP: Hemispheric Transport of Air Pollution 2010 (Executive Summary). Available online
786 from: http://www.htap.org/publications/2010_report/2010_Final_Report/EBMeeting2010.pdf
787 (Accessed 26 February 2013), 2010.

788 Hubanks, P. A., King, M. A., Platnick, S., and Pincus, R.: MODIS atmosphere L3 gridded
789 product algorithm theoretical basis document, MODIS Algorithm Teoretical Basis Document
790 No. ATBD-MOD-30 ,available at: http://modis-
791 atmos.gsfc.nasa.gov/_docs/L3_ATBD_2008_12_04.pdf,2008.

792 Koch, D., Schulz, M., Kinne, S., McNaughton, C., Spackman, J. R., Balkanski, Y., Bauer, S.,
793 Berntsen, T., Bond, T. C., Boucher, O., Chin, M., Clarke, A., De Luca, N., Dentener, F.,
794 Diehl, T., Dubovik, O., Easter, R., Fahey, D. W., Feichter, J., Fillmore, D., Freitag, S., Ghan, S.,
795 Ginoux, P., Gong, S., Horowitz, L., Iversen, T., Kirkevåg, A., Klimont, Z., Kondo, Y., Krol, M.,
796 Liu, X., Miller, R., Montanaro, V., Moteki, N., Myhre, G., Penner, J. E., Perlwitz, J., Pitari, G.,
797 Reddy, S., Sahu, L., Sakamoto, H., Schuster, G., Schwarz, J. P., Seland, Ø., Stier, P.,
798 Takegawa, N., Takemura, T., Textor, C., van Aardenne, J. A., and Zhao, Y.: Evaluation of black
799 carbon estimations in global aerosol models, Atmos. Chem. Phys., 9, 9001-9026,
800 doi:10.5194/acp-9-9001-2009, 2009

801

802 Kurata, G., Carmichael, G. R., Streets, D. G., Kitada, T., Tang,Y., Woo, J. H., and
803 Thongboonchoo, N.: Relationships between emission sources and air mass characteristics in East
804 Asia during the TRACE-P period, Atmos. Environ., 38(40), 6977–6987, 2004.

805 Levy, R. C., Remer, L. A., Mattoo, S., Vermote, E. F. and Kaufman, Y. J.: Second-generation
806 operational algorithm: Retrieval of aerosol properties over land from inversion of Moderate
807 Resolution Imaging Spectroradiometer spectral reflectance, J Geophys Res-Atmos , 112(D13),
808 D13211, doi:10.1029/2006JD007811, 2007.

809 Lu, Z., Zhang, Q. and Streets, D. G.: Sulfur dioxide and primary carbonaceous aerosol emissions
810 in China and India, 1996–2010, Atmos Chem Phys, 11(18), 9839–9864, doi:10.5194/acp-11-
811 9839-2011 Available online from: http://www.atmos-chem-phys.net/11/9839/2011/), 2011.

812 Miller-Schulze, J. P., Shafer, M. M., Schauer, J. J., Solomon, P. a., Lantz, J., Artamonova, M.,
813 Chen, B., Imashev, S., Sverdlik, L., Carmichael, G. R. and Deminter, J. T.: Characteristics of
814 fine particle carbonaceous aerosol at two remote sites in Central Asia, Atmos Environ, 45(38),
815 6955–6964, doi:10.1016/j.atmosenv.2011.09.026, 2011.

816

817 Park, S., Martin M. Shafer, James J. Schauer, Paul A. Solomon, Jeffrey Lantz, Maria
818 Artamonova, Boris Chen, Sanjar Imashev, Leonid Sverdlik, Greg R. Carmichael: Chemical
819 characteristics, dynamics and provenance of mineral dust observed at two sites in Central Asia,
820 Atmos. Environ., in preparation,2014.

821 Ramanathan, V. and Carmichael, G.: Global and regional climate changes due to black carbon,
822 Nat Geosci, 1(4), 221–227 Available online from:
823 http://www.nature.com/ngeo/journal/vaop/ncurrent/full/ngeo156.html (Accessed 18 February
824 2013), 2008.

825 Remer, L. A., Kaufman, Y. J., Tanré, D., Mattoo, S., Chu, D. A., Martins, J. V, Li, R.-R., Ichoku,
826 C., Levy, R. C., Kleidman, R. G., Eck, T. F., Vermote, E., and Holben, B.N.: The MODIS
827 aerosol algorithm products and validation, J. Atmos. Sci., 62, 947–973, doi:10.1175/JAS3385.1,
828 2005.

829 Skamarock, W. C., Klemp, J. B., Dudhia, J., Gill, D. O., Barker, D. M., Duda, M. G., Huang,
830 X.- Y., Wang, W., and Powers, J. G.: A Description of the Advanced Research WRF, Version 3.
831 Technical Report NCAR/TN475+ST R. National Center for Atmospheric Research Technical
832 Note, Boulder, Colorado, 2008.

833 Shindell, D., Kuylenstierna, J. C. I., Vignati, E., van Dingenen,R., Amann, M., Klimont, Z.,
834 Anenberg, S. C., Muller, N.,Janssens-Maenhout, G., Raes, F., Schwartz, J., Faluvegi, G.,Pozzoli,
835 L, Kupiainen, K., Hoglund-Isaksson, L., Emberson, L., Streets, D., Ramanathan, V., Hicks, K.,
836 Kim Oanh, N. T., Milly, G., Williams, M., Demkine, V., and Fowler, D: Simultaneously
837 mitigating near-term climate change and improving human health and food security, Science,
838 335, 183–189, doi:10.1126/science.1210026 , 2012.

UNEP: Framework Convention on Environmental Protection for Sustainable Development in Central Asia, Regional Resource Centre for Asia and the Pacific (PRC.AP), available at: http://www.rrcap.ait.asia/library/ca-report/Brief-Convention.doc, (last access: 25 April 2014), 2006.

UNEP and WMO: Integrated Assessment of Black Carbon and Tropospheric Ozone: Summary for Decision Makers. available at: http://www.unep.org/dewa/Portals/67/pdf/BlackCarbon_SDM.pdf (last access: 26 February 2013), 2011.

Uno, I., Satake, S., Carmichael, G. R., Tang, Y., Wang, Z., Takemura, T., Sugimoto, N., Shimizu, A., Murayama, T., Cahill, T.A., Cliff, S., Uematsu, M., Ohta, S., Quinn, P. K., and Bates, T.S.: Numerical study of Asian dust transport during the springtime of 2001 simulated with the Chemical Weather Forecasting System (CFORS) model, J. Geophys. Res., 109(D19S24), doi:10.1029/2003JD004222, 2004.

V Visschedijk, A., Denier van der Gon, H., Droge, R.,van der Brugh, H.: A European high resolution and size-differentiated emission inventory for elemental and organic carbon for the year 2005, TNO-034-UT-2009-00688_RPT-ML, TNO, Utrecht, 2009

Wang, W., Bruyere, C., Duda, M., Dudhia, J., Gill, D., Lin, H.-C., Michalakes, J., Rizvi, S. and Zhang, X.: Version 3 Modeling System User ' s Guide January 2011, National Center for Atmospheric Research (NCAR), available at: http://www.mmm.ucar.edu/wrf/users/docs/user_guide_V3.2/ARWUsersGuideV3.pdf (last access: 25 April 2014), 2011.

Wesely, M. L. and Hicks, B. B.: A review of the current status of knowledge on dry deposition, Atmos Environ, 34(12–14), 2261–2282, doi:http://dx.doi.org/10.1016/S1352-2310(99)00467-7, 2000.

Whish-Wilson, P.: The Aral Sea environmental health crisis the desiccation of the Aral Sea health in the Aral Sea region, Journal of Rural and Remote Environmental Health,1(2), 29–34, available at: http://www.jcu.edu.au/jrtph/vol/v01whish.pdf (last access: 25 April 2014), 2002.

Wiedinmyer, C., Akagi, S. K., Yokelson, R. J., Emmons, L. K., Al-Saadi, J. a., Orlando, J. J. and Soja, a. J.: The Fire INventory from NCAR (FINN): a high resolution global model to estimate the emissions from open burning, Geoscientific Model Development, 4(3), 625–641, doi:10.5194/gmd-4-625-2011, 2011.

Zhang, Q., Streets, D. G., Carmichael, G. R., He, K. B., Huo, H., Kannari, A., Klimont, Z., Park, I. S., Reddy, S., Fu, J. S., Chen, D., et al.: Asian emissions in 2006 for the NASA INTEX-B mission., Atmos Chem Phys, 9(14/2), 5131–5153, doi:10.5194/acp-9-5131-2009, 2009.

7. Table Captions

Table:1 Summary of changes in Central Asia (CA) region (See figure 1 for CA region definition) emissions and concentration under the future emission scenarios (See Sect. 3.8 for more details)

8. Figure Captions

Fig. 1. WRF-STEM modeling domain set up and source region definition used in the simulations. Modeling analysis was done on the hemispheric scale. The black dotted rectangular box denotes the subset of the modeling domain used in this analysis. The triangle and circle markers denote locations of the LST and Bishkek observation sites. The anthropogenic source regions are denoted by colored regions with the A notation: A1 (N. America), A2 (Europe), A3 (Russia), A4 (Middle East), A5 (Central Asia), A6 (China) and A7 (South + Southeast Asia). The dust source regions are indicated by the magenta rectangles with the D notations: D1 (Africa), D2 (Middle East), D3 (Central Asia) and D4 (Western China). The biomass burning sources regional boundaries are indicated by the long dashed black lines with B notations: B1 (N. America i.e. region west of 25 W), B2 (Europe i.e. region west of 45E and 40 N and above), B3 (Siberia : i.e east of 45 E and 40 N and above) and B4 (South Asia i.e. below 40 N). The insert shows the topography around the observation sites.

Fig. 2. Spatial distribution of a) BC b) SO_2 c) Natural dust d) Biomass burning $PM_{2.5}$ emissions averaged over the simulation period in Gg/yr/grid.

Fig. 3. Spatial distribution of MODIS AOD averaged over the simulation period. The triangle and circle markers denote the location of LST and Bishkek sites. The numbers on the map denote contour values at sharp gradients.

Fig. 4. Spatial distribution of simulated a) BC ($\mu g/m^3$), b) Dust ($\mu g/m^3$), c) $PM_{2.5}$ ($\mu g/m^3$), and d) AOD averaged over the simulation period. The values on the map denote contour values at sharp gradients.

Fig. 5. Comparison of predicted meteorological variables from WRF model with observations shown as box and whisker plots over the simulation period (a) Temperature (K), (b) Relative Humidity RH (%), (c) Wind Speed (m/s), (d) Wind Direction (°), and (e) PBL height (m). Lidar denotes the LST (Lidar Station Teplokluchenka) site. In each box whisker panel, the middle line denotes the median value, while the edges of the box represent 25th and 75th percentile values respectively. The whiskers denote the maximum and minimum values.

Fig. 6. Comparison of predicted aerosols with observations shown as box and whisker plots over the simulation period at a) LST and b) Bishkek sites. SP and LE denote the AOD from the sun-photometer (SP) and integrated fromthe vertical extinction profiles (LE). OBS and TEOM denote filter and TEOM measurements while the MDL denotes the modeled values respectively. Lidar denotes the LST (Lidar Station Teplokluchenka) site. In each box whisker panel, the middle line denotes the median value, while the edges of the box represent 25th and 75th

911 percentile values respectively. The whiskers denote the maximum and minimum values. The
912 triangle marker denotes the mean value.

913 Fig. 7. Summary of period mean contributions by source regions and sectors for AOD, $PM_{2.5}$,
914 dust, non-dust $PM_{2.5}$, sulfate and BC in % for the grid cells containing the Bishkek and LST
915 observation sites, and spatially averaged over the Central Asia region. See Fig. 1 for
916 anthropogenic, dust and fire source regions. Lidar denotes the LST (Lidar Station
917 Teplokluchenka) site.

918 Fig. 8. Temporal variability in simulated AOD compared with observations at the LST site. The
919 box-plots of monthly values are shown. AOD from the sun-photometer (SP) and integrated from
920 the vertical extinction profiles (LE) are shown. MDL denotes modeled values. Lidar denotes the
921 LST (Lidar Station Teplokluchenka) site. In each box whisker panel, the middle line denotes the
922 median value, while the edges of the box represent 25th and 75th percentile values respectively.
923 The whiskers denote the maximum and minimum values.

924 Fig. 9. Comparison of simulated PM mass with filter-based observations at Central Asia sites (a)
925 $PM_{2.5}$ (LST) along with TEOM non-volatile measurements, (b) $PM_{2.5}$ (Bishkek), (c) PM_{10} (LST),
926 and (d) PM_{10} (Bishkek) in ($\mu g/m^3$). Lidar denotes the LST (Lidar Station Teplokluchenka) site.

927 Fig. 10. Temporal variability in simulated (a) Temperature (K) and (b) Relative Humidity RH
928 (%) from WRF model compared with observations at the LST and Bishkek sites. Lidar denotes
929 the LST (Lidar Station Teplokluchenka) site.

930 Fig. 11. Simulated composition of $PM_{2.5}$ at the LST site by a) Species ($\mu g/m^3$), b) Fine dust
931 source regions($\mu g/m^3$) c) Anthropogenic $PM_{2.5}$ source regions ($\mu g/m^3$) d) Anthropogenic $PM_{2.5}$
932 source ($\mu g/m^3$) e) Biomass $PM_{2.5}$ source regions($\mu g/m^3$).The contributions from source region
933 and sectors denote the non – dust portion of $PM_{2.5}$ mass.

934 Fig. 12. Simulated composition of BC at the LST site by a) Source regions ($\mu g/m^3$), b) Source
935 sector ($\mu g/m^3$), and c) Biomass burning source regions ($\mu g/m^3$).

936 Fig. 13. Time altitude cross sections of weekly averaged predicted BC, dust and $PM_{2.5}$ for the
937 simulation period at the LST site. The numbers denote the specific episodes of aerosol
938 enhancements for back trajectory analysis in Fig. 14 and Fig. 15. Lidar denotes the LST (Lidar
939 Station Teplokluchenka) site.

940 Fig. 14. Ten day air mass back trajectories for August 2008 (events 1 and 2 as denoted in Fig.
941 13) color coded by source regions. The blue diamond and green square hatched areas denote the
942 natural dust and biomass burning emission sources while the number in black denote MODIS
943 AOD contours averaged over the event time period and ten day prior time window. The
944 trajectories are color coded by source regions including Africa (blue), Middle East (green),
945 Central Asia (yellow), North Asia biomass (> 50° N, black), Europe (brown), China (red) and
946 South Asia (orange). Lidar denotes the LST (Lidar Station Teplokluchenka) site.

947 Fig. 15. Same as Fig. 14 but for November 2008, January 2009 and April 2009 (events 3, 4, 5
948 denoted in Fig. 13).

949 Fig. 16 Ten day air mass forward trajectories illustrating the seasonality in transport pathways
950 out of CA for a) June 2008, b) December 2008, and c) April 2009. The blue diamond, green
951 square hatched areas denote the natural dust and biomass burning emission sources while the
952 number in black denote MODIS AOD contours, respectively, averaged over the event time
953 period and subsequent ten day time window. Lidar denotes the LST (Lidar Station
954 Teplokluchenka) site.

955 Fig. 17. Seasonally averaged surface total dust (PM_{10}) concentrations from Central Asia dust
956 emissions. DJF (top left panel) denotes the average for the months of December, January and
957 February. MAM (top right panel) denotes the average for months of March, April and May. JJA
958 (bottom left panel) denotes the average for months of June, July and August while SON (bottom
959 right panel) denotes average for months of September, October and November.

960 Fig. 18. Time series of predicted surface concentration at 6 h time step (top panel) and weekly
961 averaged time altitude cross sections (bottom panel) of total dust (PM_{10}) from Central Asia dust
962 emissions at Mt. Bachelor, Oregon.

963 Fig. 19. Percent change in simulated period mean surface BC and $PM_{2.5}$ concentrations for future
964 2030 emission scenarios relative to the base year (2005) a),d) reference 2030, a),e) BC measures
965 (low) and c),f) BC (lowest) and greenhouse gas measures aimed at keeping CO_2 levels below
966 450 ppm. Refer to Sec. 2.3 for more details on emission scenarios.

967

968 **9. Supplemental Materials Figure and Table Captions**

969 Table S1. Comparison of the observed and predicted surface meteorology at the observation
970 sites.

971 Table S2. Comparison of observations and model of AOD, $PM_{2.5,}$ PM_{10}, BC and OC at the
972 Bishkek site.

973 Table S3. Comparison of observations and model of AOD, $PM_{2.5,}$ PM_{10}, BC and OC at the LST
974 site.

975

976 Fig. S1. Seasonal variability in spatial distribution of biomass burning $PM_{2.5}$ emissions in
977 Gg/month/grid (a) April 2008, (b) August 2008, (c) November 2008, and (d) May 2009.

978 Fig. S2. Spatial distribution of a) base year 2005 BC emissions (Gg/yr/grid) along with percent
979 change (w.r.t to base year 2005) in b) Reference 2030 BC emissions c) 2030 BC emissions with
980 BC measures (low) and d) 2030 BC emissions with BC (lowest) and greenhouse gas measures
981 aimed at keeping CO_2 levels below 450ppm. The triangle and circle markers denote locations of
982 the LST and Bishkek sites. Refer to Sec. 2.3 for more details on emission scenarios.

983 Fig. S3. Spatial distribution of a) base year 2005 $PM_{2.5}$ emissions (Gg/yr/grid) along with percent
984 change (w.r.t to base year 2005) in b) Reference 2030 $PM_{2.5}$ emissions c) 2030 $PM_{2.5}$ emissions
985 with BC measures and d) 2030 $PM_{2.5}$ emissions with BC and greenhouse gas measures aimed at

keeping CO_2 levels below 450ppm. The triangle and circle markers denote locations of the LST and Bishkek sites. Refer to Sec. 2.3 for more details on emission scenarios.

Fig. S4. Spatial distribution of a) base year 2005 SO_2 emissions (Gg/yr/grid) along with percent change (w.r.t to base year 2005) in (b) Reference 2030 SO_2emissions c) 2030 SO_2 emissions with BC measures and d) 2030 SO_2 emissions with BC and greenhouse gas measures aimed at keeping CO_2 levels below 450ppm. The triangle and circle markers denote locations of the LST and Bishkek sites. Refer to Sec. 2.3 for more details on emission scenarios.

Fig. S5. Comparison of observed and predicted PBL heights (m) at the LST site. Observed PBL heights were determined from the Lidar profiles.

Fig. S6. Spatial distribution of predicted species contributions (%) to AOD averaged over the simulation period a) Carbonaceous aerosols (BC+OC), b) SO4, c) Other PM, and d) Dust.

Fig. S7. Spatial distribution of predicted species contributions (%) to $PM_{2.5}$ averaged over the simulation period a) Carbonaceous aerosols (BC+OC), b) SO4, c) Other $PM_{2.5}$, and d) Dust.

Fig. S8. Seasonal variability in spatial distribution of MODIS and simulated AOD averaged over the simulation period.

Fig S9. Summary of period mean contributions by source regions and sectors for OC in % for the grid cells containing the Bishkek and LST observation sites, and spatially averaged over the Central Asia region. See Fig. 1 for anthropogenic and fire source regions.

1004 Table:1 Summary of changes in Central Asia (CA) region (See figure 1 for CA region definition)
1005 emissions and concentration under the future emission scenarios (See Sect. 3.8 for more details)
1006

Emission Scenario	**Emissions Gg yr^{-1}**			**Emissions change (%) w.r.t to base 2005**		
	BC	SO_2	PM_{25}	BC	SO_2	PM_{25}
Base 2005	39	1130	197			
Reference 2030	47	1326	224	22.1	17.3	13.9
Low GWP 2030	27	1325	177	-31.1	17.3	-10.1
Lowest GWP + 450	21	1058	115	-46.9	-6.4	-41.5

	Concentration (µg m^{-3})			**Concentration change (%) w.r.t to base 2005**		
	BC	SO_4	PM_{25}	BC	SO_4	$PM_{2.5}$
Base 2005	0.17	3.04	4.26			
Reference 2030	0.16	2.65	4.03	-4.2	-12.6	-5.3
Low GWP 2030	0.11	2.64	3.85	-36.6	-13	-9.5
Lowest GWP + 450	0.10	2.04	3.06	-38.5	-32.9	-28

1007

1008

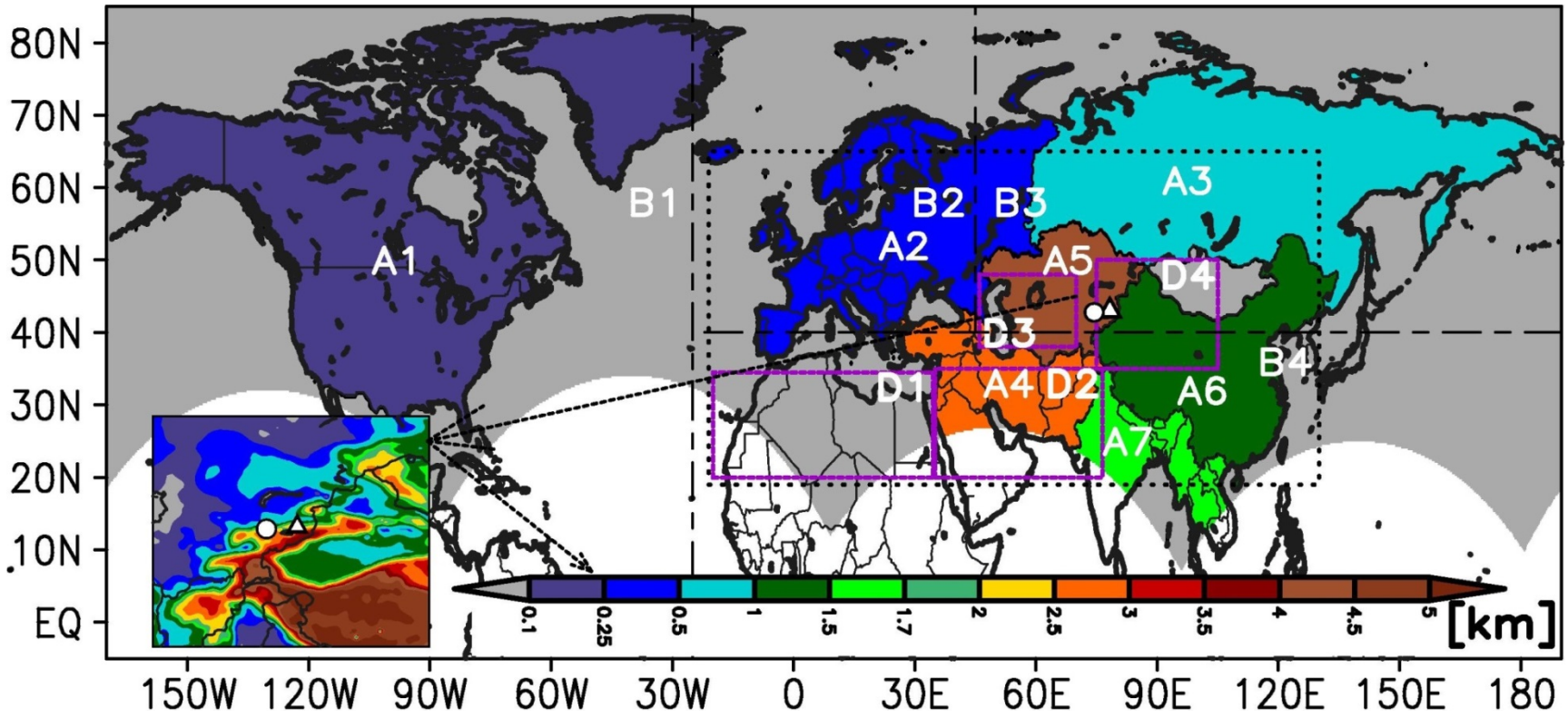

Fig. 1. WRF-STEM modeling domain set up and source region definition used in the simulations. Modeling analysis was done on the hemispheric scale. The black dotted rectangular box denotes the subset of the modeling domain used in this analysis. The triangle and circle markers denote locations of the LST and Bishkek observation sites. The anthropogenic source regions are denoted by colored regions with the A notation: A1 (N. America), A2 (Europe), A3 (Russia), A4 (Middle East), A5 (Central Asia), A6 (China) and A7 (South + Southeast Asia). The dust source regions are indicated by the magenta rectangles with the D notations: D1 (Africa), D2 (Middle East), D3 (Central Asia) and D4 (Western China). The biomass burning sources regional boundaries are indicated by the long dashed black lines with B notations: B1 (N. America i.e. region west of 25 W), B2 (Europe i.e. region west of 45E and 40 N and above), B3 (Siberia : i.e east of 45 E and 40 N and above) and B4 (South Asia i.e. below 40 N). The insert shows the topography around the observation sites.

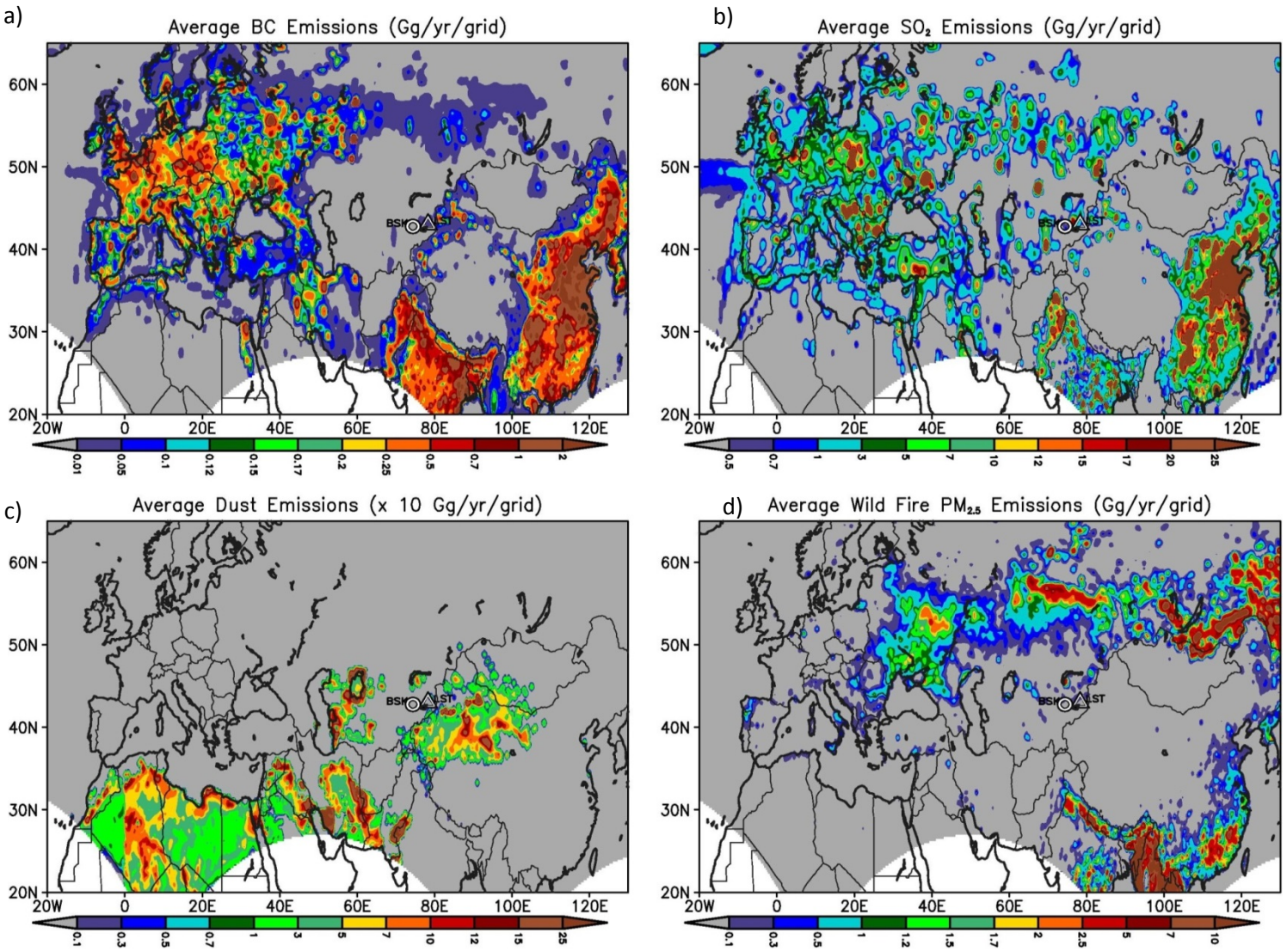

Fig. 2. Spatial distribution of a) BC b) SO_2 c) Natural dust d) Biomass burning $PM_{2.5}$ emissions averaged over the simulation period in Gg/yr/grid.

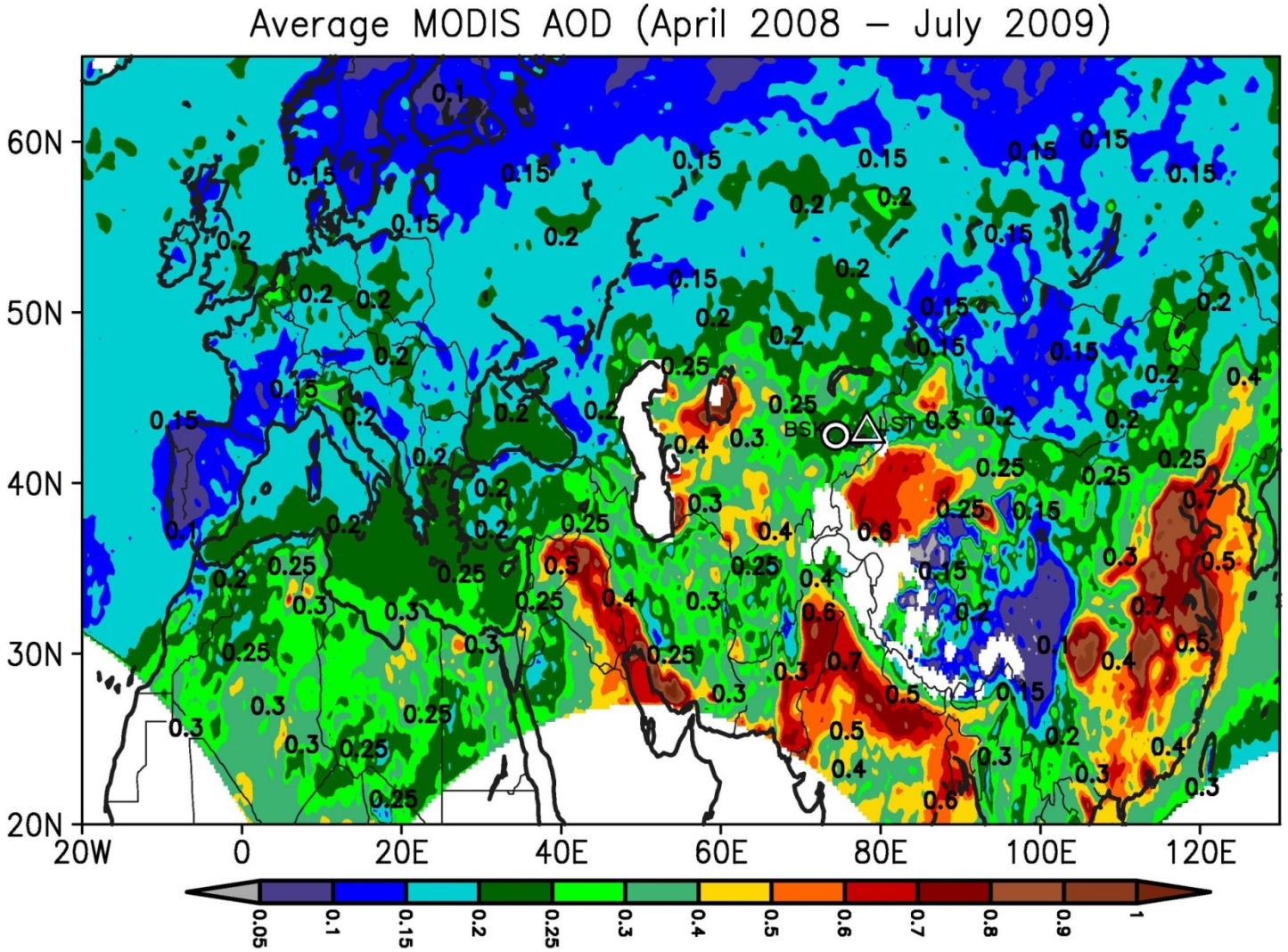

Fig. 3. Spatial distribution of MODIS AOD averaged over the simulation period. The triangle and circle markers denote the location of LST and Bishkek sites. The numbers on the map denote contour values at sharp gradients.

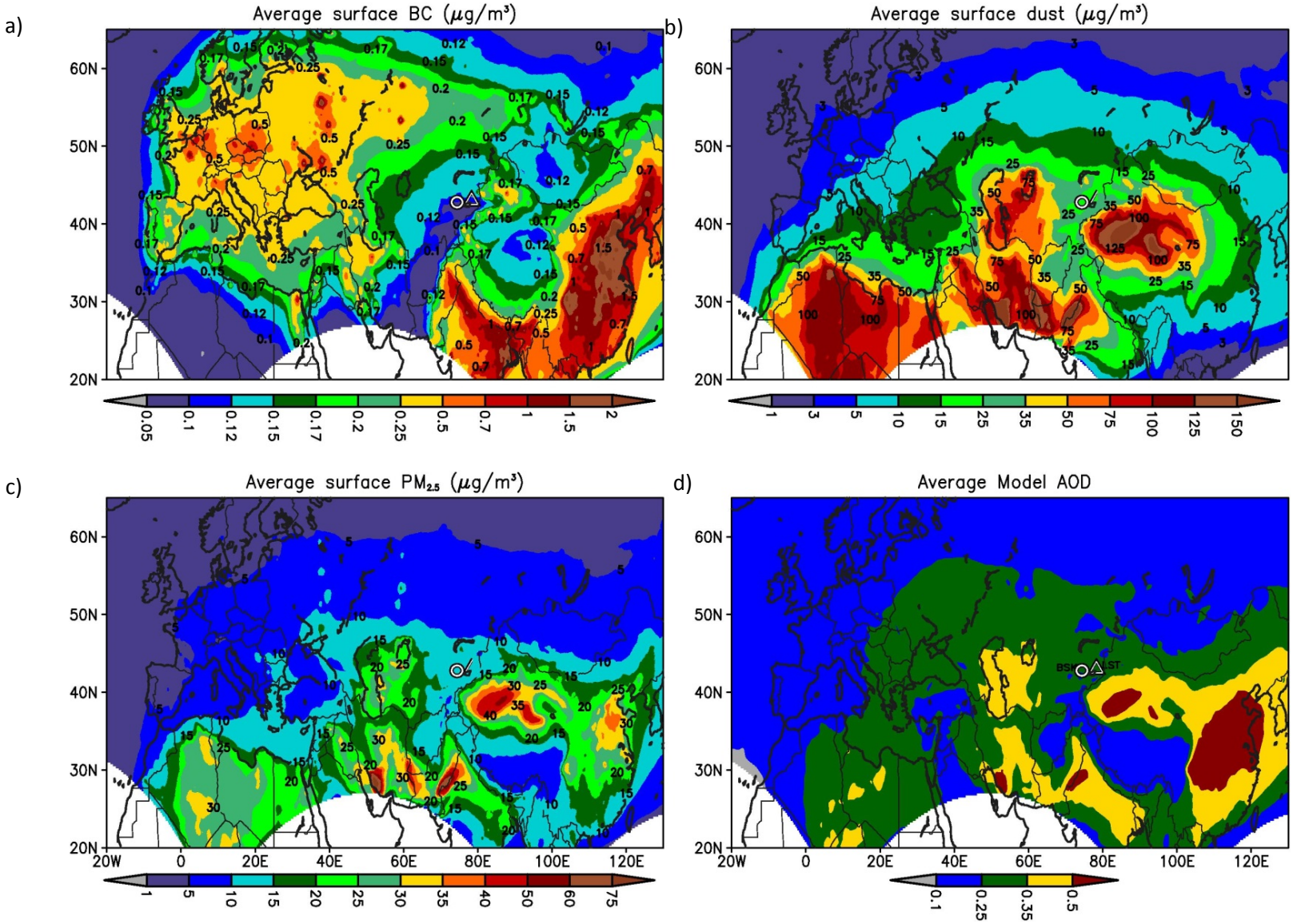

Fig. 4. Spatial distribution of simulated a) BC (μg/m^3), b) Dust (μg/m^3), c) $PM_{2.5}$ (μg/m^3), and d) AOD averaged over the simulation period. The values on the map denote contour values at sharp gradients.

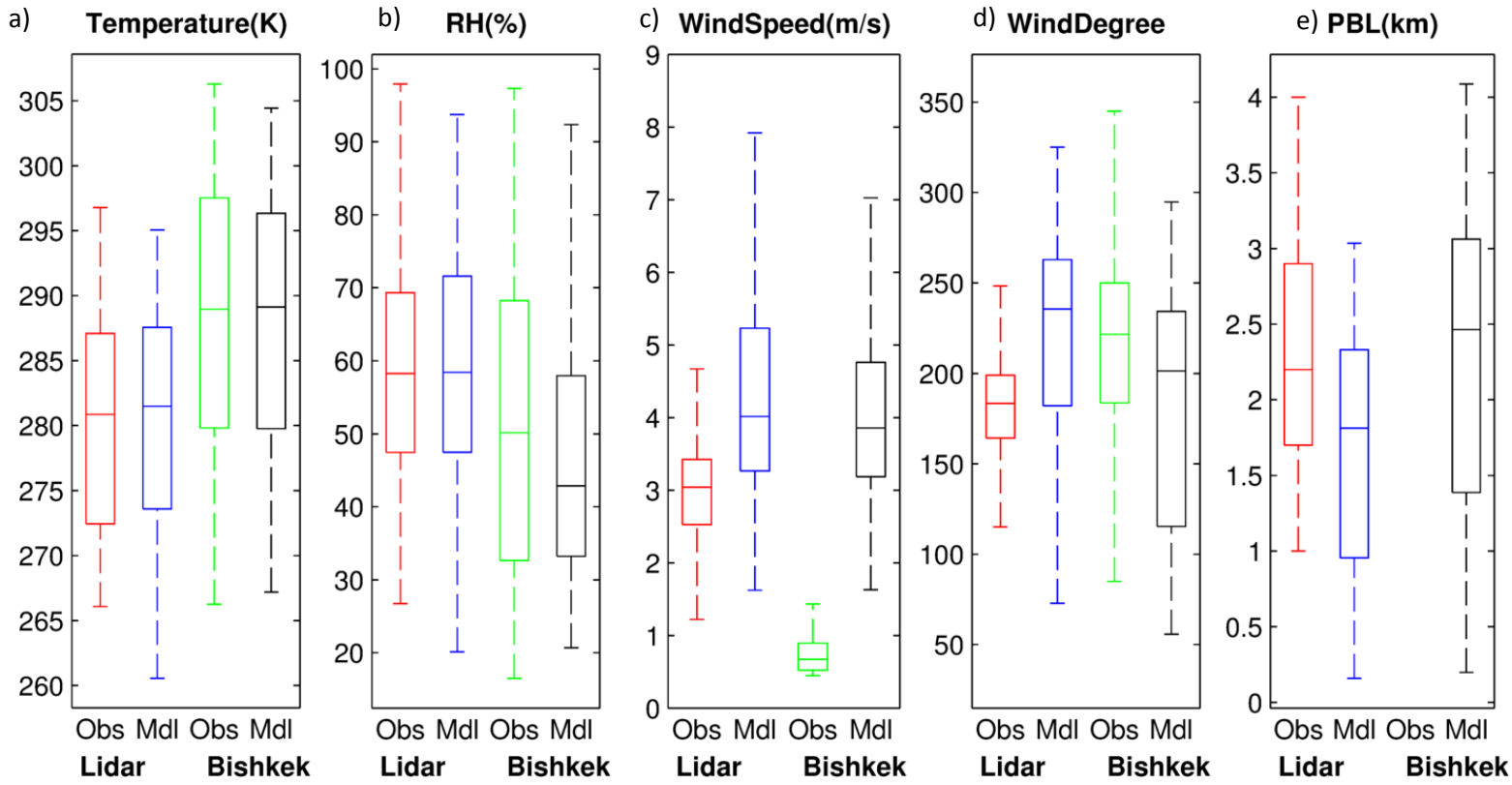

Fig. 5. Comparison of predicted meteorological variables from WRF model with observations shown as box and whisker plots over the simulation period (a) Temperature (K), (b) Relative Humidity RH (%), (c) Wind Speed (m/s), d) Wind Direction (°), and PBL height (m). Lidar denotes the LST (Lidar Station Teplokluchenka) site. In each box whisker panel, the middle line denotes the median value, while the edges of the box represent 25th and 75th percentile values respectively. The whiskers denote the maximum and minimum values.

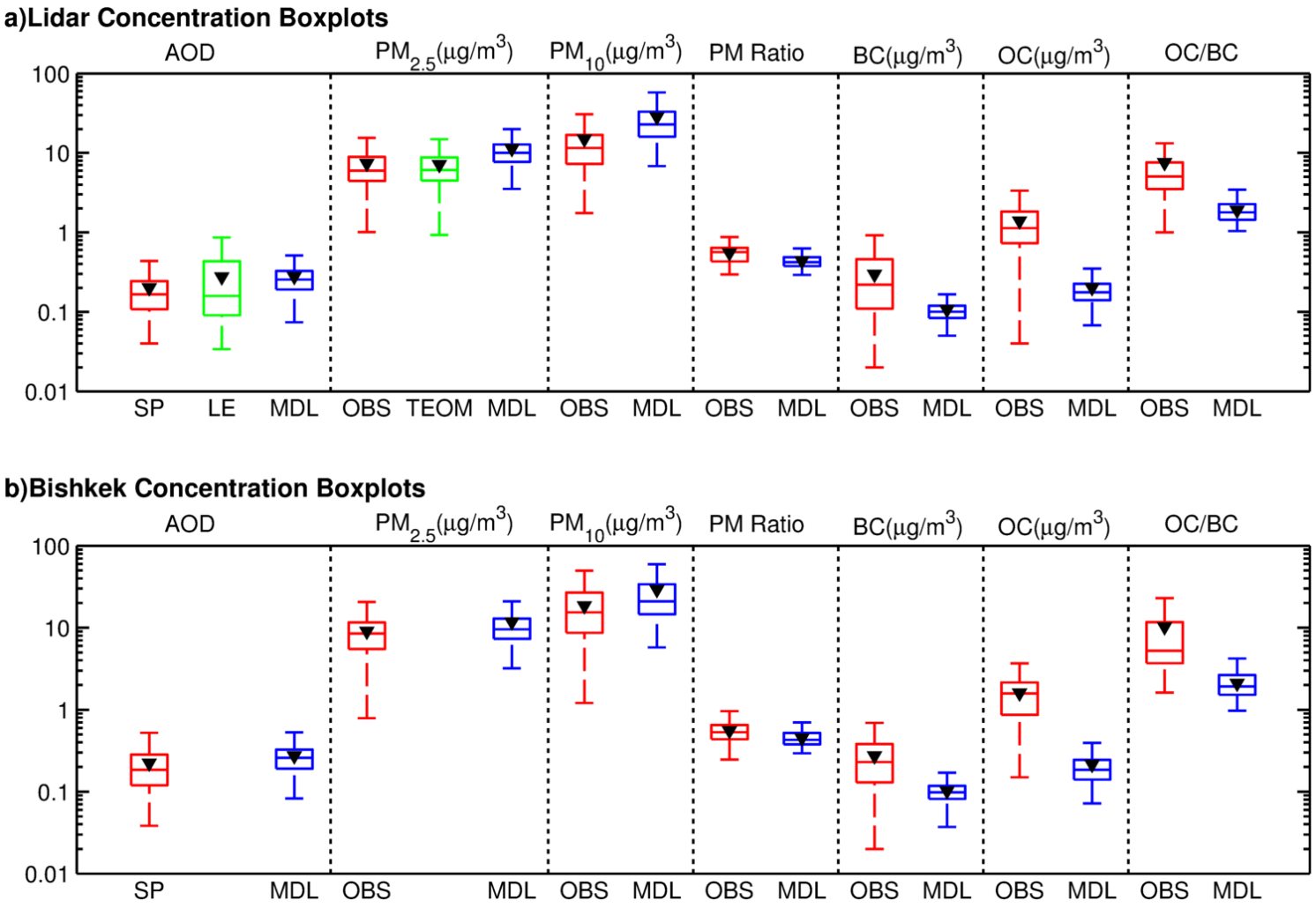

Fig. 6. Comparison of predicted aerosols with observations shown as box and whisker plots over the simulation period at a) LST and b) Bishkek sites.SP and LE denote the AOD from the sun-photometer (SP) and integrated from the vertical extinction profiles (LE). OBS and TEOM denote filter and TEOM measurements while the MDL denotes the modeled values respectively. Lidar denotes the LST (Lidar Station Teplokluchenka) site. In each box whisker panel, the middle line denotes the median value, while the edges of the

box represent 25th and 75th percentile values respectively. The whiskers denote the maximum and minimum values. The triangle marker denotes the mean value.

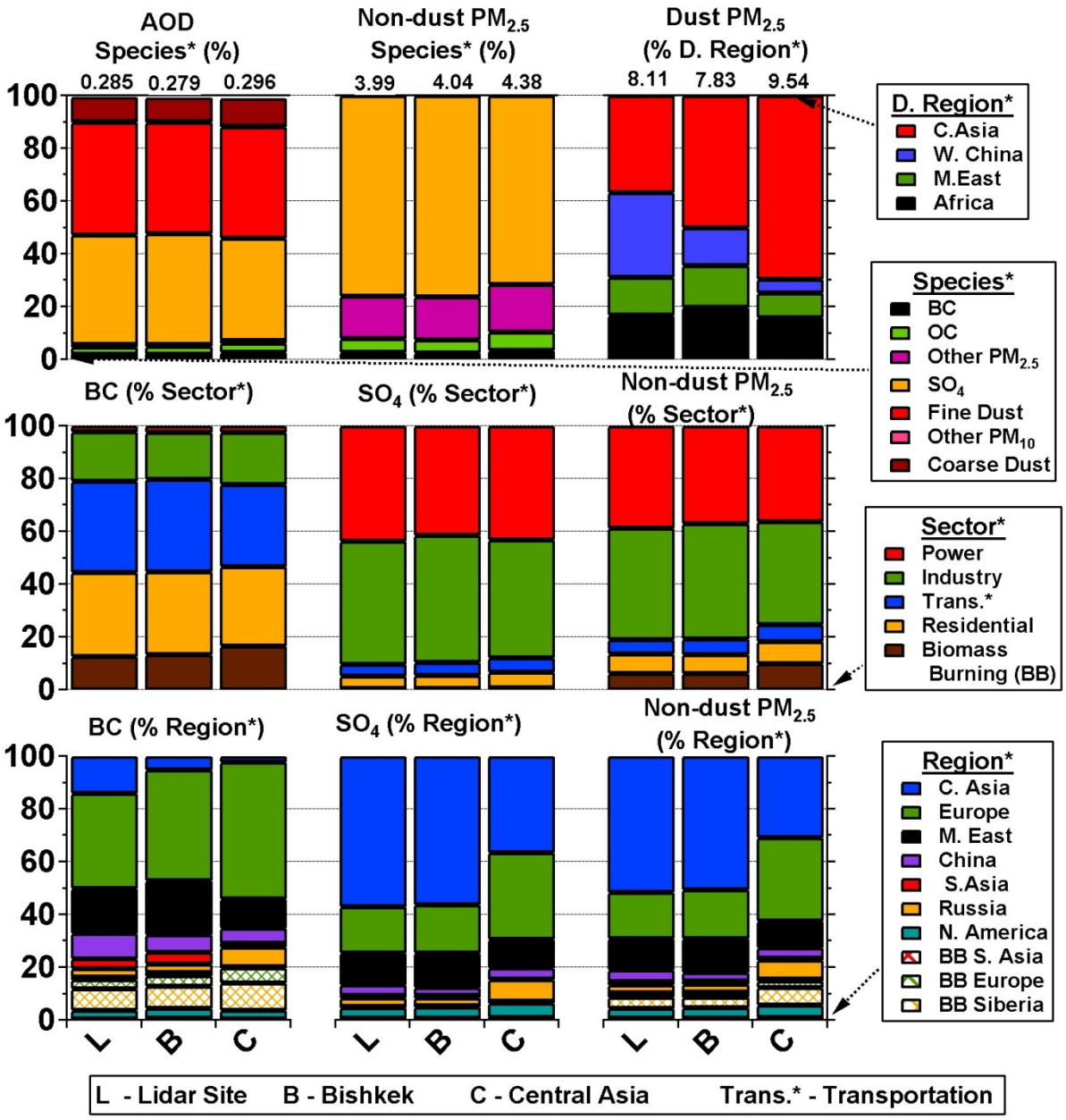

Fig. 7. Summary of period mean contributions by source regions and sectors for AOD, $PM_{2.5}$, dust, non-dust $PM_{2.5}$, sulfate and BC in % for the grid cells containing the Bishkek and LST observation sites, and spatially averaged over the Central Asia region. See Fig. 1 for anthropogenic, dust and fire source regions. Lidar denotes the LST (Lidar Station Teplokluchenka) site.

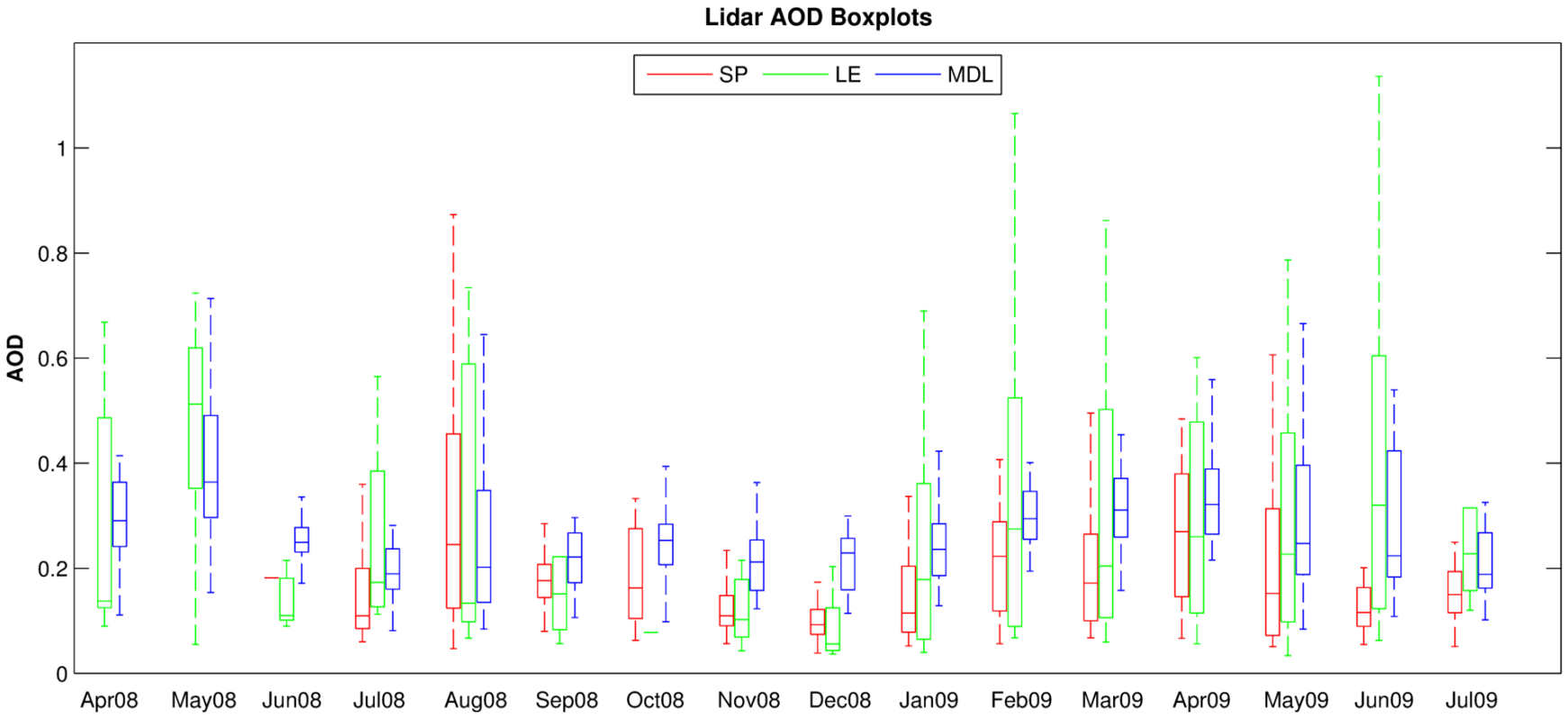

Fig. 8. Temporal variability in simulated AOD compared with observations at the LST site. The box-plots of monthly values are shown. AOD from the sun-photometer (SP) and integrated from the vertical extinction profiles (LE) are shown. MDL denotes modeled values. Lidar denotes the LST (Lidar Station Teplokluchenka) site. In each box whisker panel, the middle line denotes the median value, while the edges of the box represent 25th and 75th percentile values respectively. The whiskers denote the maximum and minimum values.

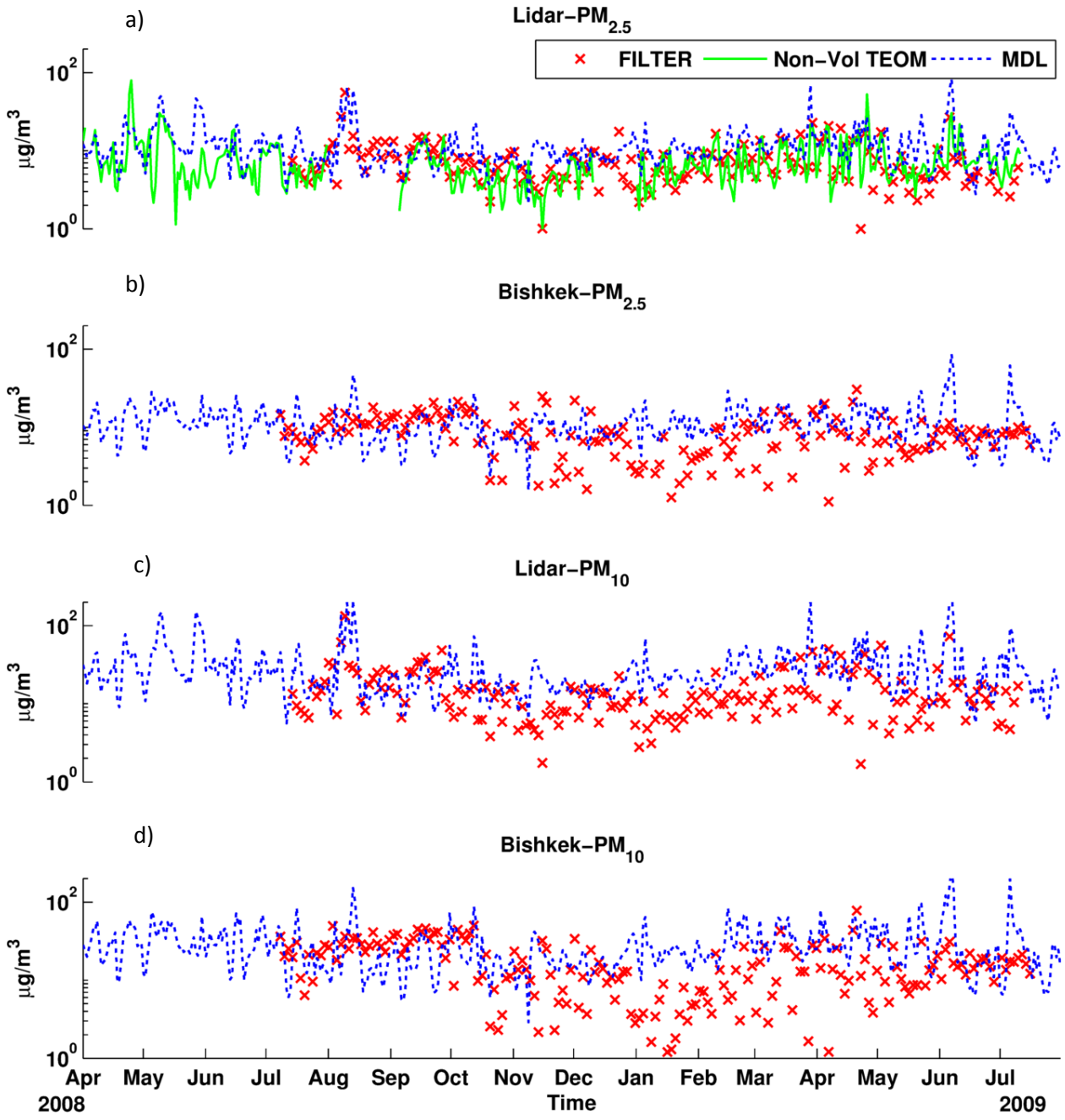

Fig. 9. Comparison of simulated PM mass with filter-based observations at Central Asia sites (a) $PM_{2.5}$ (LST) along with TEOM non-volatile measurements, (b) $PM_{2.5}$ (Bishkek), (c) PM_{10} (LST), and (d) PM_{10} (Bishkek) in (µg/m^3). Lidar denotes the LST (Lidar Station Teplokluchenka) site.

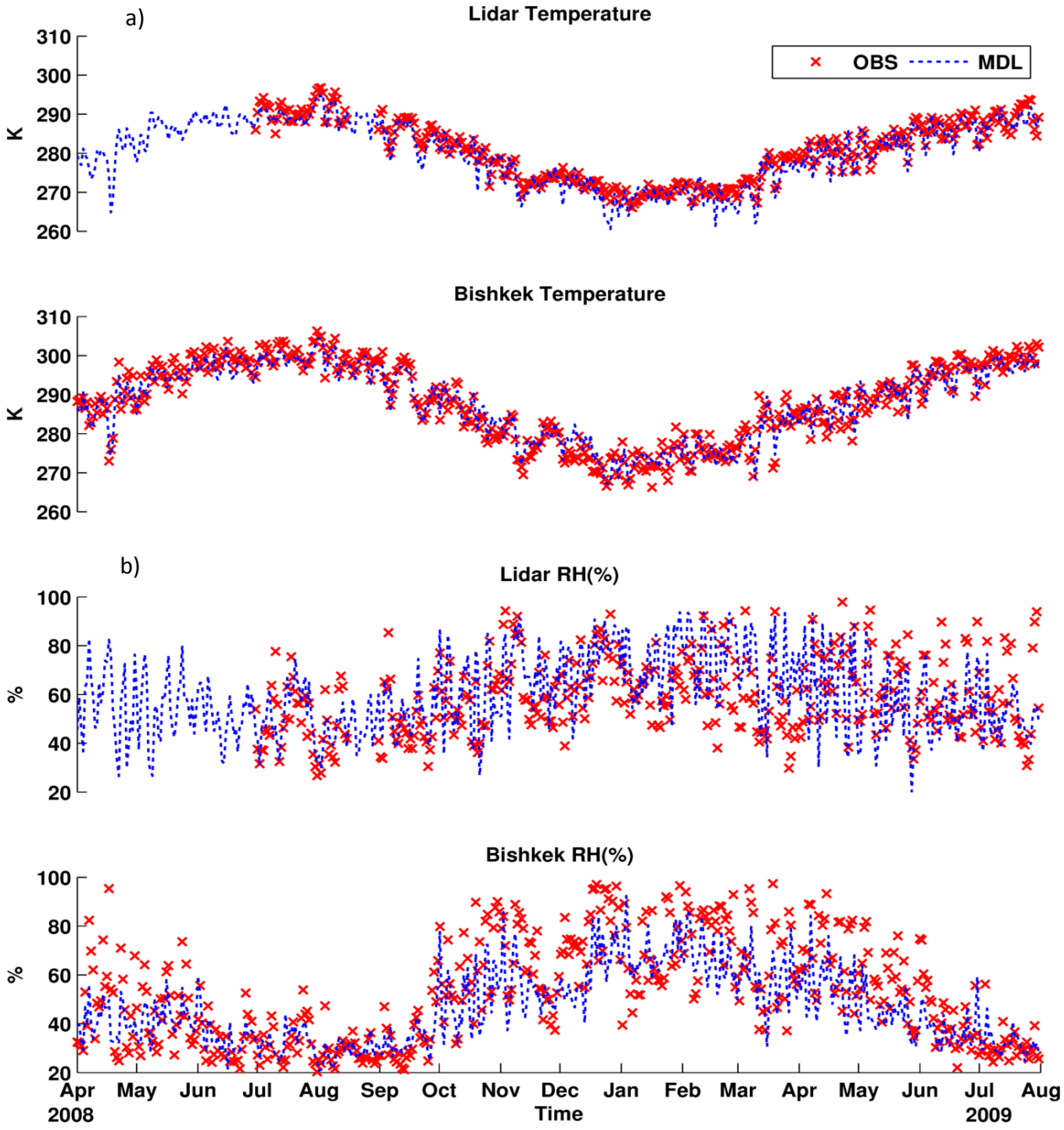

Fig. 10. Temporal variability in simulated Temperature (K) and (b) Relative Humidity RH (%) from WRF model compared with observations at the LST and Bishkek sites. Lidar denotes the LST (Lidar Station Teplokluchenka) site.

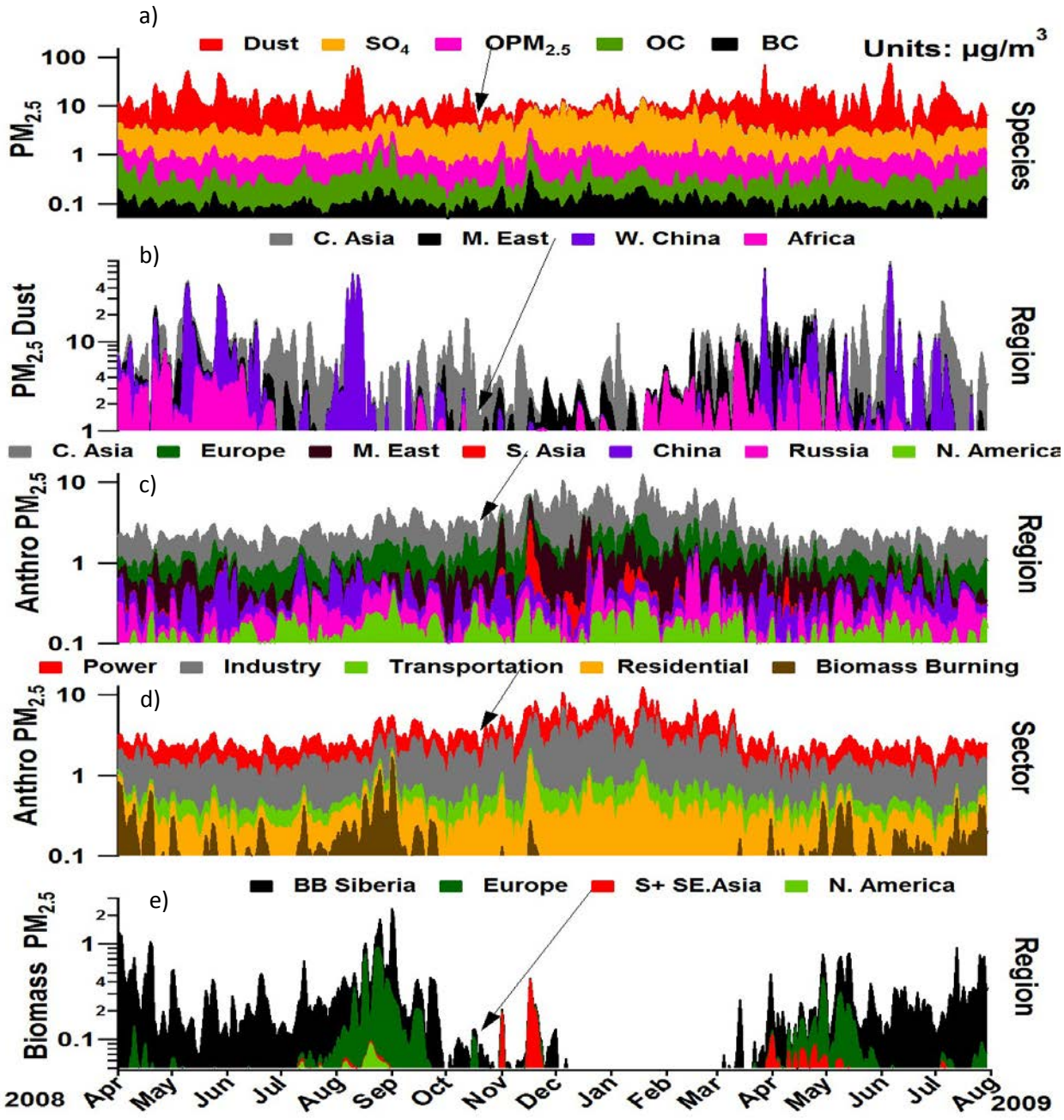

Fig. 11. Simulated composition of $PM_{2.5}$ at the LST site by a) Species (µg/m^3), b) Source sector (µg/m^3), and c) Source regions (µg/m^3). The contributions from source region and sectors denote the non – dust portion of $PM_{2.5}$ mass.

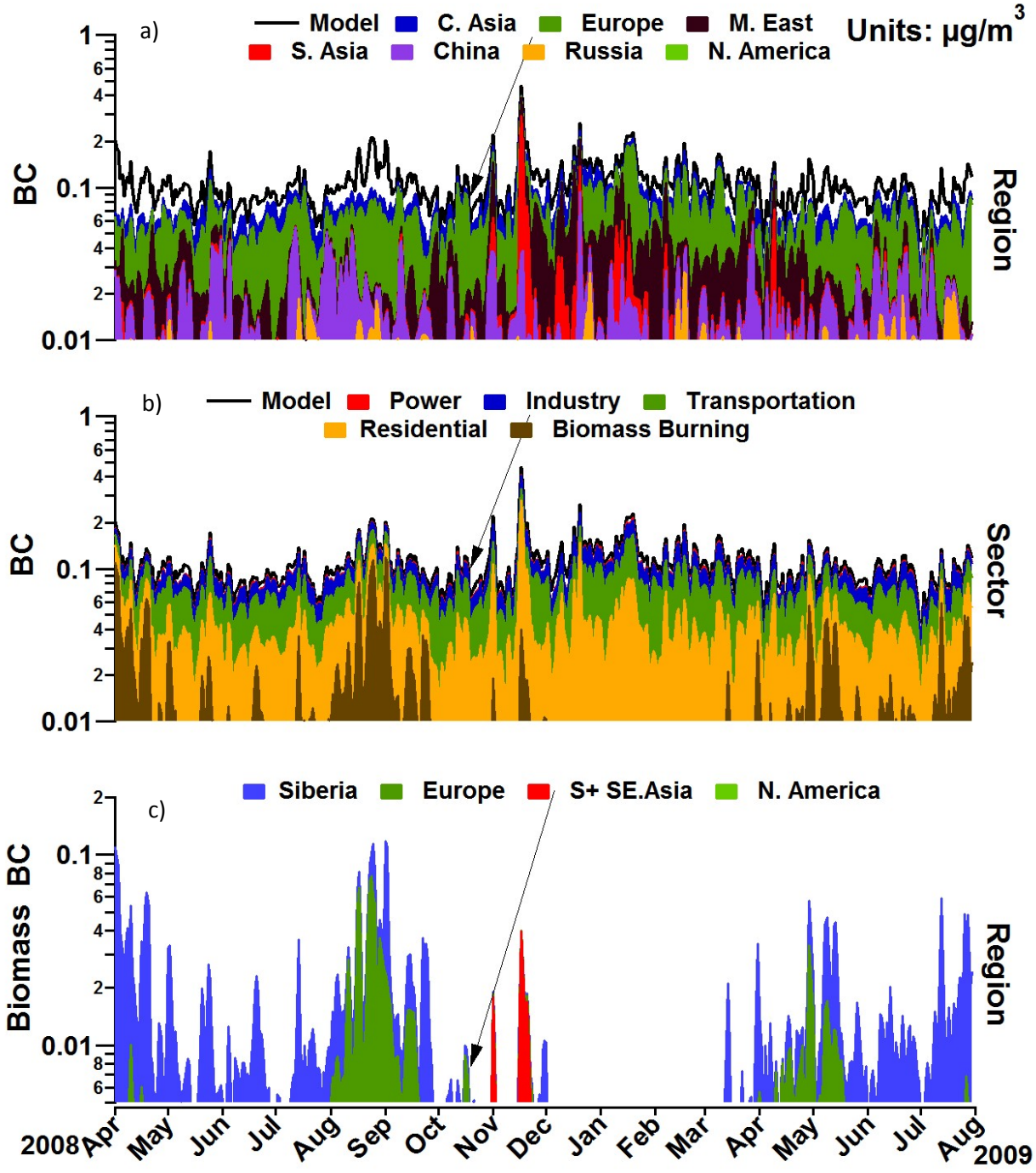

Fig. 12. Simulated composition of BC at the LST site by a) Source regions (µg/m^3), b) Source sector (µg/m^3), and c) Biomass burning source regions (µg/m^3).

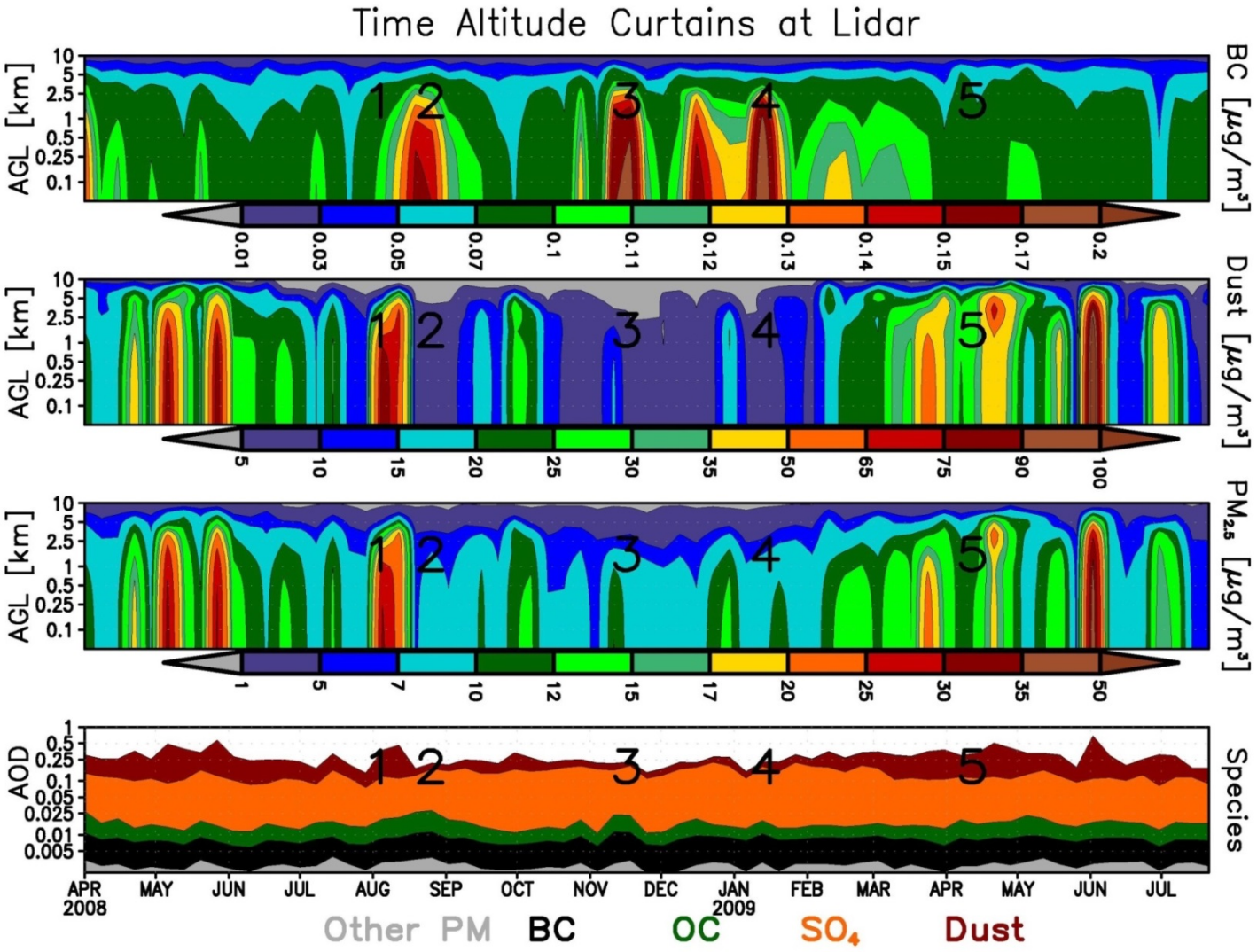
Time Altitude Curtains at Lidar
AGL [km]
BC [μg/m³]
Dust [μg/m³]
PM2.5 [μg/m³]
AOD
Species
1
2
3
4
5
APR 2008
MAY
JUN
JUL
AUG
SEP
OCT
NOV
DEC
JAN 2009
FEB
MAR
APR
MAY
JUN
JUL
Other PM
BC
OC
SO4
Dust

Fig. 13. Time altitude cross sections of weekly averaged predicted BC, dust and $PM_{2.5}$ for the simulation period at the LST site. The numbers denote the specific episodes of aerosol enhancements for back trajectory analysis in Fig. 14 and Fig. 15. Lidar denotes the LST (Lidar Station Teplokluchenka) site.

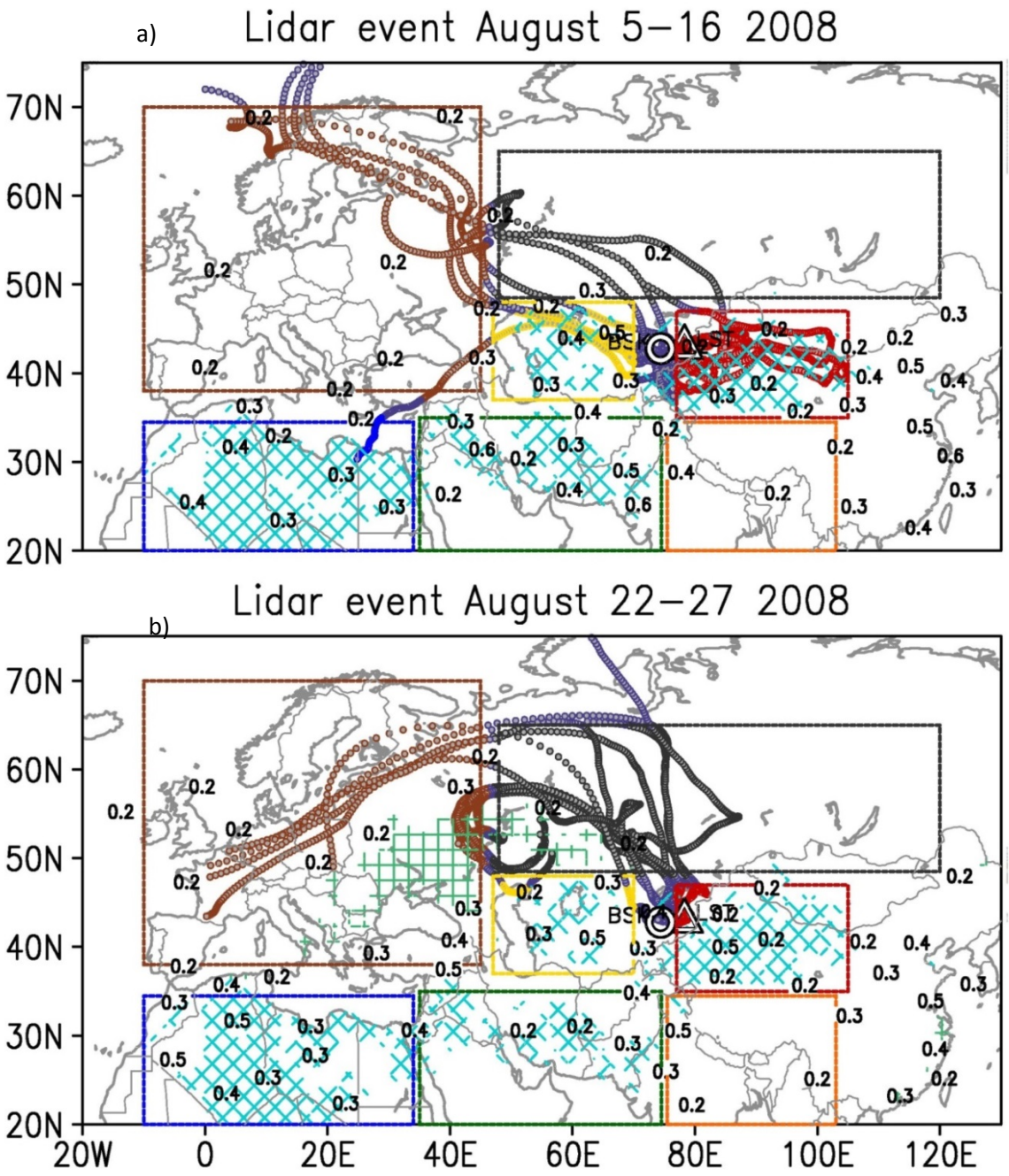

Fig. 14. Ten day air mass back trajectories for August 2008 (events 1 and 2 as denoted in Fig. 11) color coded by source regions. The blue diamond and green square hatched areas denote the natural dust and biomass burning emission sources while the number in black denote MODIS AOD contours averaged over the event time period and ten day prior time window. The trajectories are color coded by source regions including Africa (blue), Middle East (green), Central Asia (yellow), North Asia biomass (> 50° N, black), Europe (brown), China (red) and South Asia (orange). (green), Central Asia (yellow), North Asia biomass (> 50° N,

black), Europe (brown), China (red) and South Asia (orange). Lidar denotes the LST (Lidar Station Teplokluchenka) site.

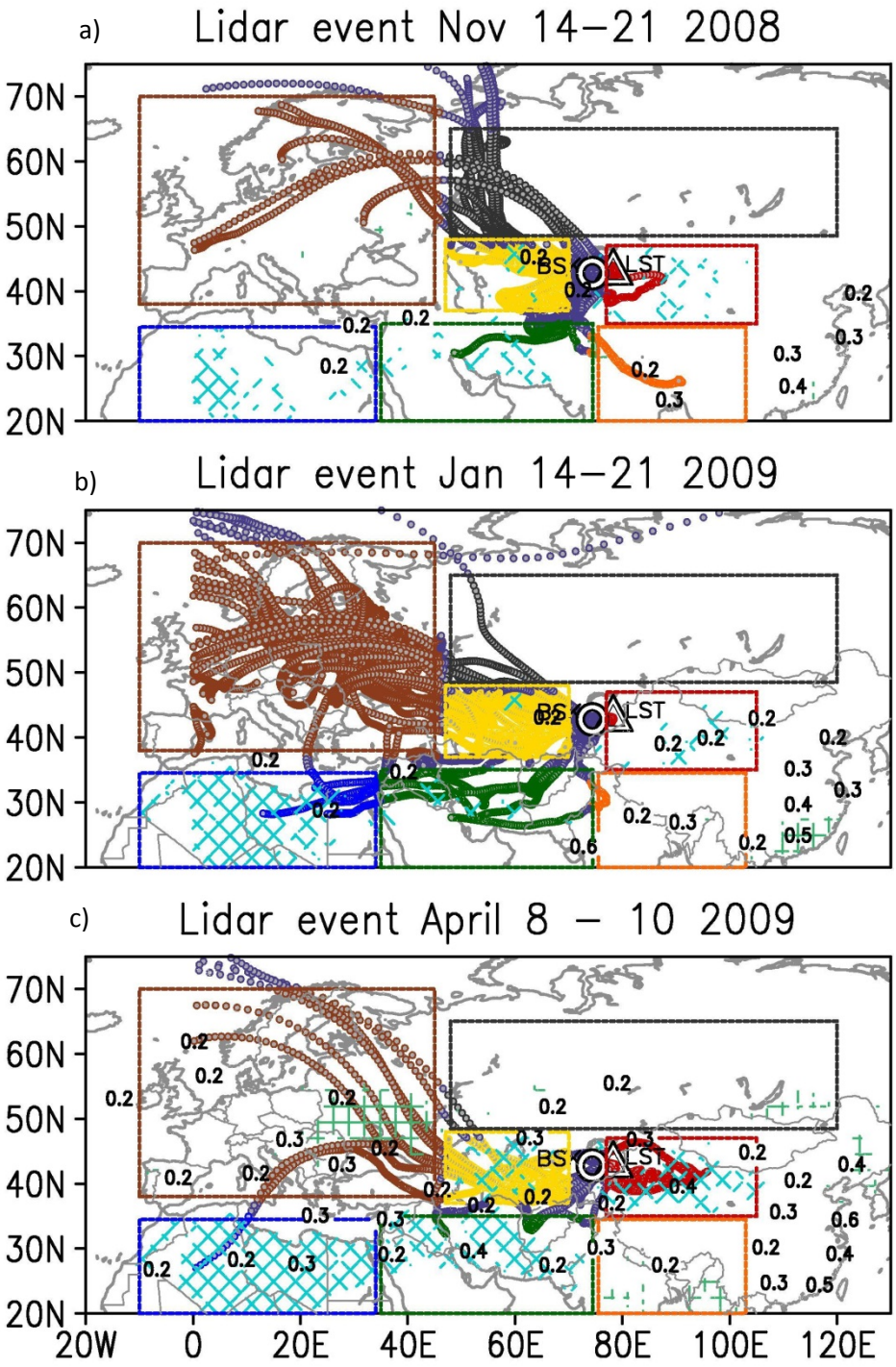

Fig. 15. Same as Fig. 14 but for November 2008, January 2009 and April 2009 (events 3, 4, 5 denoted in Fig. 13).

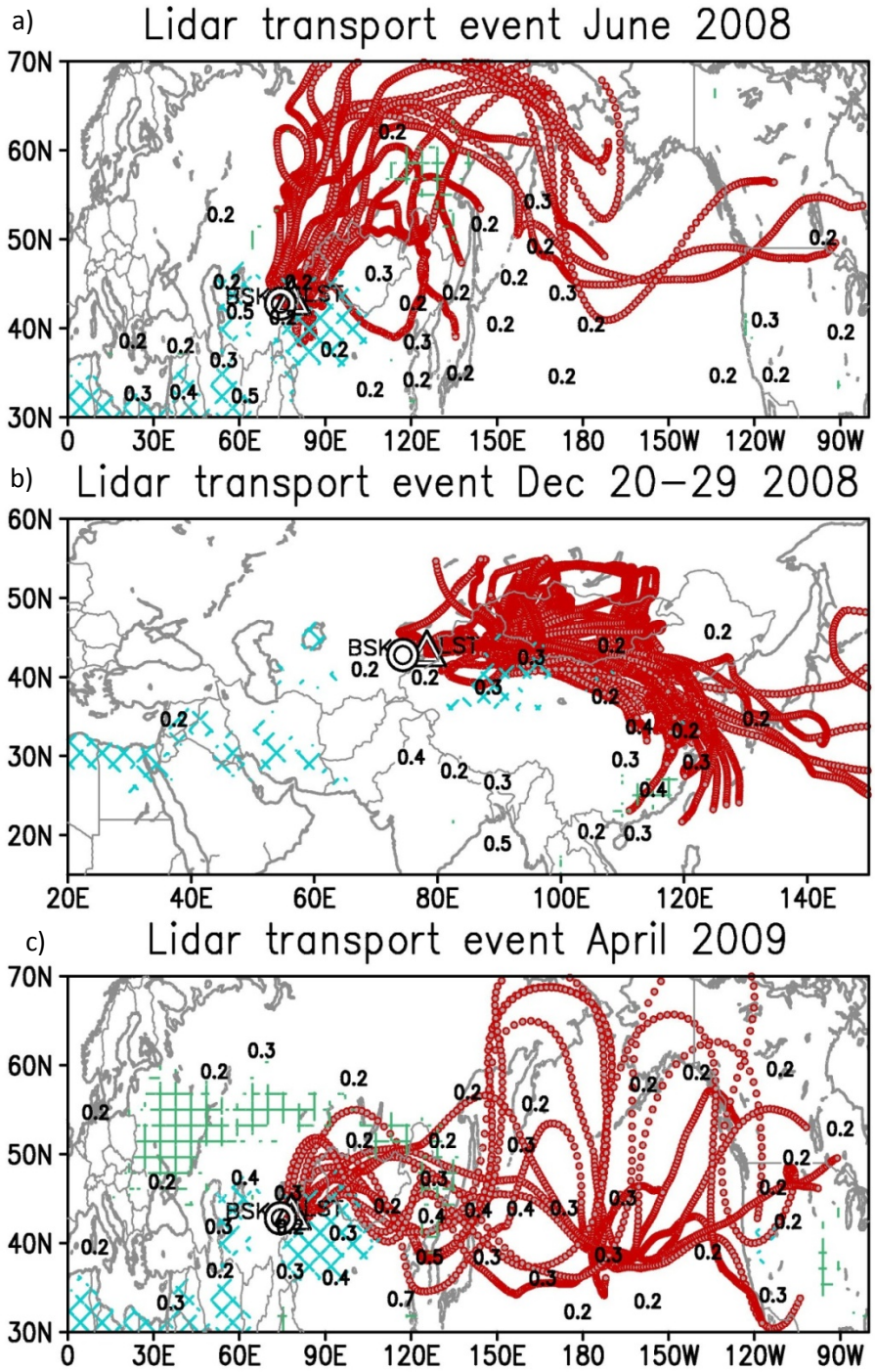

Fig. 16 Ten day air mass forward trajectories illustrating the seasonality in transport pathways out of CA for a) June 2008, b) December 2008, and c) April 2009. The blue diamond, green square hatched areas denote the natural dust and biomass burning emission sources while the number in black denote MODIS AOD contours, respectively, averaged over the event time

period and subsequent ten day time window. Lidar denotes the LST (Lidar Station Teplokluchenka) site.

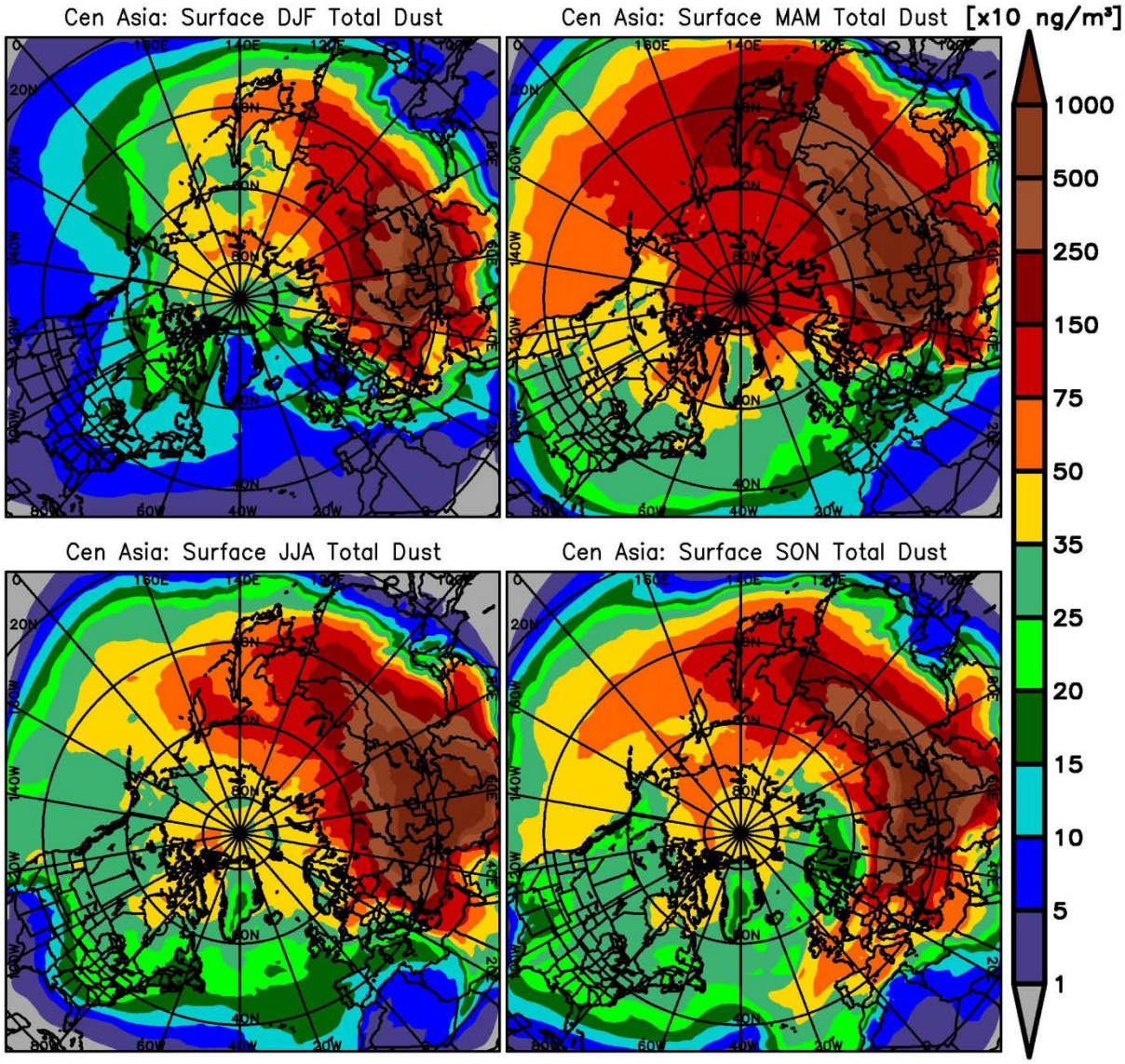

Fig. 17. Seasonally averaged surface total dust (PM_{10}) concentrations from Central Asia dust emissions. DJF (top left panel) denotes the average for the months of December, January and February. MAM (top right panel) denotes the average for months of March, April and May. JJA (bottom left panel) denotes the average for months of June, July and August while SON (bottom right panel) denotes average for months of September, October and November.

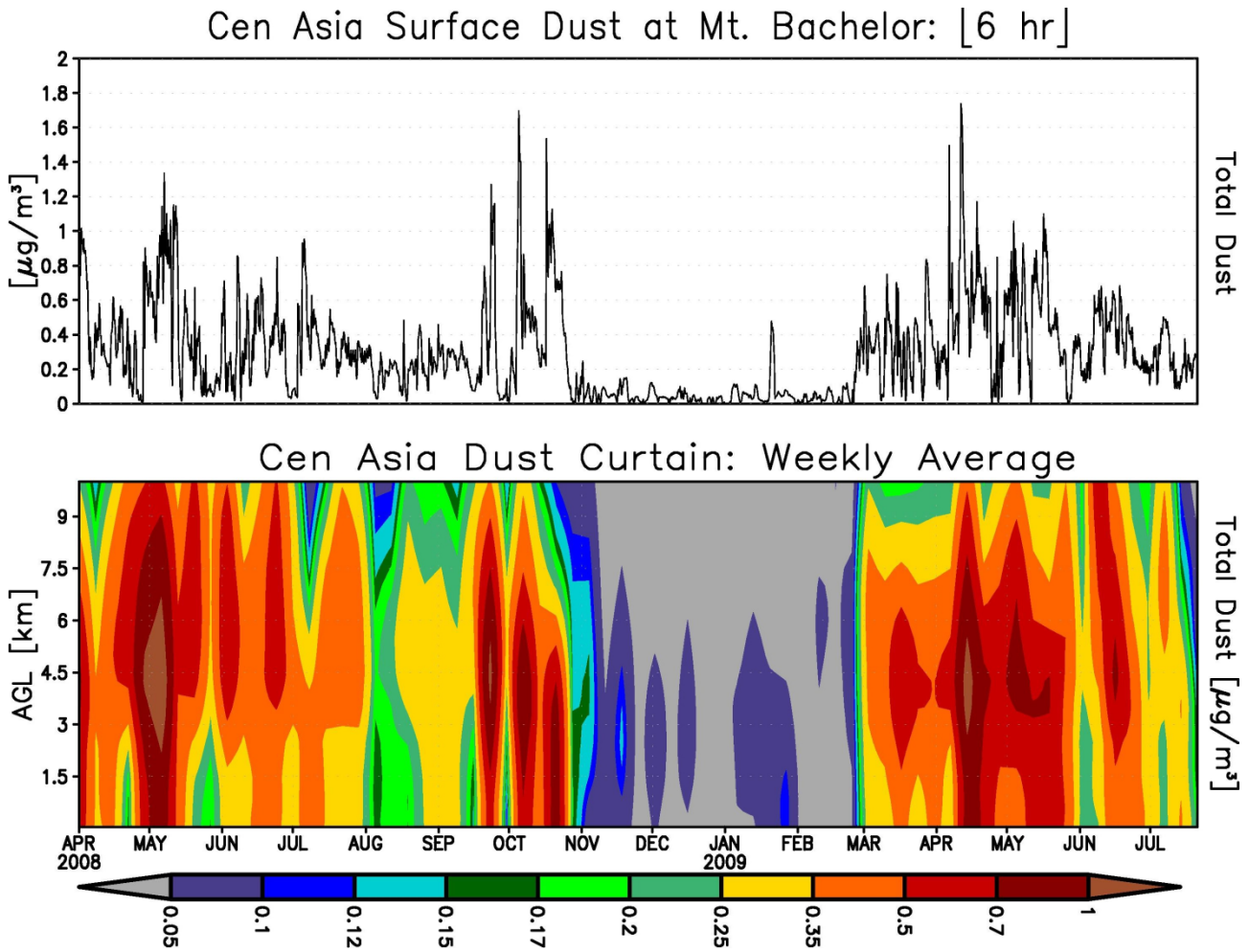

Fig. 18. Time series of predicted surface concentration at 6 h time step (top panel) and weekly averaged time altitude cross sections (bottom panel) of total dust (PM_{10}) from Central Asia dust emissions at Mt. Bachelor, Oregon.

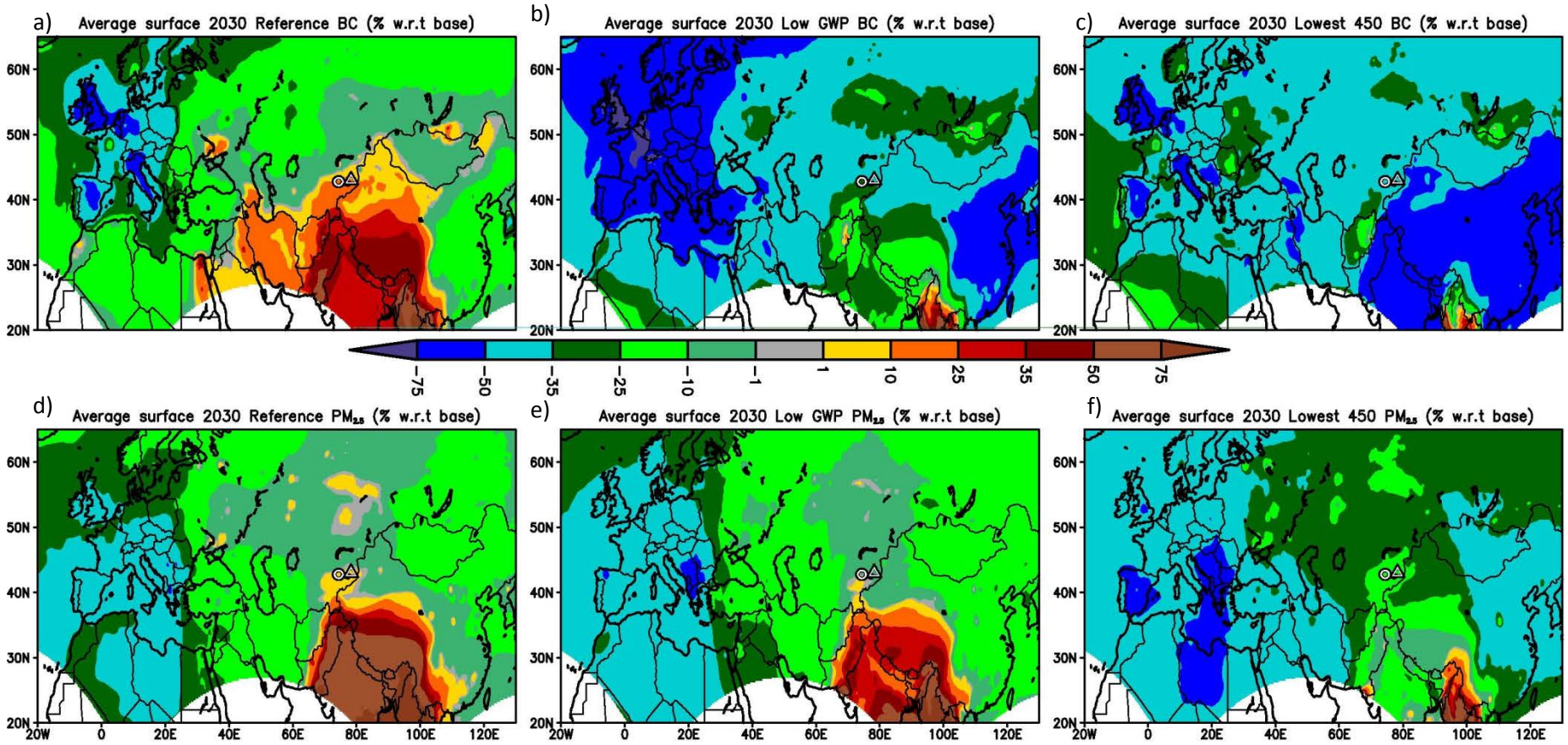

Fig. 19. Percent change in simulated period mean surface BC and $PM_{2.5}$ concentrations for future 2030 emission scenarios relative to the base year (2005) a),d) reference 2030, a),e) BC measures (low) and c),f) BC (lowest) and greenhouse gas measures aimed at keeping CO_2 levels below 450 ppm. Refer to Sec. 2.3 for more details on emission scenarios.